arXiv:1701.00610v1 [physics.data-an] 3 Jan 2017

Change detection in complex dynamical systems using intrinsic phase and amplitude synchronization

Ashif Sikandar Iquebal[1], Satish Bukkapatnam[1], and Arun Srinivasa[2]

[1]Department of Industrial and Systems Engineering, Texas A&M University

[2]Department of Mechanical Engineering, Texas A&M University

Abstract: We present an approach for real-time change detection in the transient phases of complex dynamical systems based on tracking the local phase and amplitude synchronization among the components of a univariate time series signal derived via Intrinsic Time scale Decomposition (ITD)–a nonlinear, non-parametric analysis method. We investigate the properties of ITD components and show that the expected level of phase synchronization at a given change point may be enhanced by more than 4 folds when we employ multiple intrinsic components. Next, we introduce a concept of maximal mutual agreement to identify the set of ITD components that are most likely to capture the information about dynamical changes of interest, and define an InSync statistic to capture this local information. Extensive numerical as well as real-world case studies involving benchmark neurophysiological processes and industrial machine sensor data suggest that the present method can detect sharp change points and second/higher order moment shifts with average sensitivity of 91% as compared to approximately 30% for other contemporary methods tested on the case studies presented.

Keywords: Phase synchronization, Change detection, Nonlinear and nonstationary systems

1 Introduction

Streaming time series data is becoming increasingly available across various engineering and medical domains, particularly with the recent advances in wearable technologies and the so-called Internet of Things (IoT). This introduces new challenges and opportunities for change detection, especially to discern incipient anomalies and novelties that can cause catastrophes [1–3]. For example, early stages of debilitating physiological disorders and salient neuro-physical activity transitions can be detected using Electroencephalogram (EEG) signals [4], and defects and faults in critical components, such as large microelectronic wafers or turbine blades, can be monitored using sensor signals through out their life cycle for their quality and integrity assurance.

Existing change detection methods are essentially based on testing a hypothesis, $H_o : \boldsymbol{\theta} = \boldsymbol{\theta_0}$ against $H_a : \boldsymbol{\theta} \neq \boldsymbol{\theta_0}$ over some system parameters $\boldsymbol{\theta}$. Implicitly, these methods assume that the underlying model satisfies stationarity conditions [5] or simple forms of nonstationarity such as modulations to autocorrelation structures [6] and frequency variations [7] on the process parameters. However, real world systems manifest much

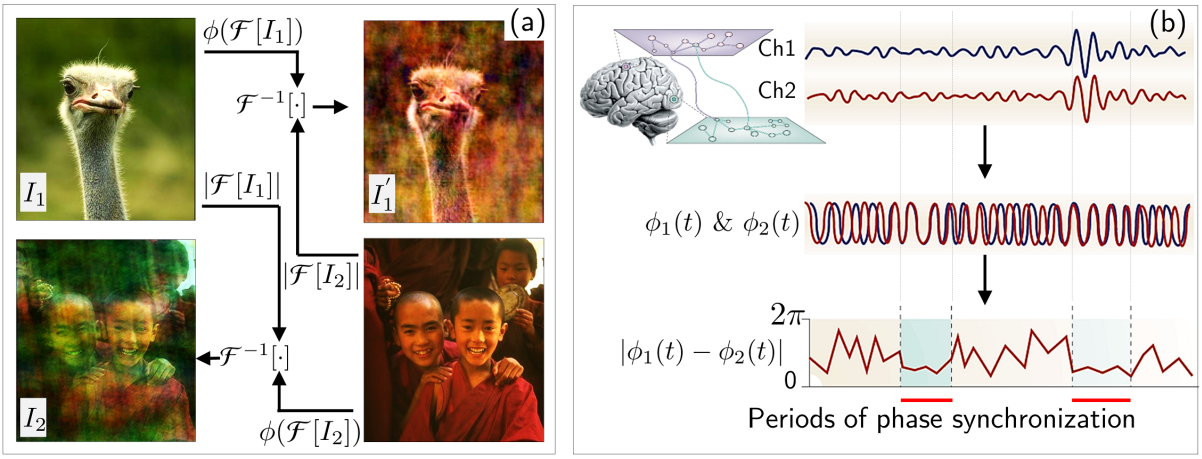

Figure 1: (a) Images reconstructed (I_1' and I_2') by swapping the phase and amplitude information of two sample images, I_1 and I_2 [16]. Here, $\phi(\cdot)$ and $|\cdot|$ represents the phase and amplitude components, respectively, of the images I_1 and I_2 in the Fourier domain ($\mathcal{F}$ being the Fourier transform). (b) shows the episodes of phase synchronization ($\triangleq |\phi_1(t) - \phi_2(t)|$) between two filtered EEG channels where phases, $\phi_1(t)$ and $\phi_2(t)$ are extracted using Hilbert transform (adapted from [13]).

more complex dynamics. Oftentimes, they exhibit nonstationary behavior referred to as intermittency, which consists of the system dynamics alternating among multiple, near-stationary regimes, resembling a piece-wise stationary process. The current change detection methods are severely limited to discern transition between different intermittent behaviors [8, 9]. Additionally, most of the existing change detection methods tend to utilize only the amplitude information [10]; phase properties of the system have not received much attention in the change detection literature [11].

The importance of phase is becoming increasingly evident in various domains, such as image analysis and reconstruction [12], neurophysiological signal analysis [13] and speech recognition [14]. For instance (see Fig. 1(a)), an image (I_1') reconstructed using the phase information from I_1 and amplitude information from I_2, resembles closer to I_1 as compared to I_2, and vice versa. The reconstruction suggests that phase preserves the "structure" of an image more so than amplitude does (see Fig. 6 in [12]). Similarly, phase-based change detection methods that utilize multiple channels of EEG data, have been used to identify the onset of neurological disorders, such as seizure [13]. For example, Fig. 1(b) shows two channels of EEG synchronously gathered from an epileptic subject prone to seizure. As the figure indicates, some of these critical events might go undetected (here, the first seizure episode) if we rely only on the amplitude information. However, these events can be accurately determined by tracking the absolute values of phase differences, ($|\phi_1(t) - \phi_2(t)|$) at each time instance t. This is because the signal phases may exhibit much higher level of synchronization compared to the corresponding amplitudes during such events [15].

In general, however, the current phase synchronization approaches need multiple signals (or channels) to utilize the phase information. In the absence of multiple signals, one needs to decompose the univariate time series signal, $x(t) \in \mathbb{R}, t \in \mathbb{Z}^+$ into multiple components to extract the phase information. Unlike stationary Gaussian time series signals obtained from linear systems, decomposition of complex nonstationary signals (e.g., EEG) is a non-trivial task. Parametric methods such as short-time Fourier, Wavelet

or Wigner-Ville transforms [17] tend to be sub-optimal (since they assume an *a priori* basis), and often yield poor or inaccurate time-frequency localization. Alternatively, non-parametric approaches, e.g., Empirical Mode Decomposition (EMD, [18]) or Independent Component Analysis offer a data driven approach (with an intrinsic basis function) for signal decomposition in nonstationary systems [2,19,20]. However, these methods cannot be used for real-time applications with streaming data because the decomposition is not causal; i.e., entire length of the signal needs to be known before the basis functions could be determined. Additionally, the sifting procedure of EMD diffuses the time-frequency-energy information across multiple decomposition levels and times for highly nonlinear systems [21].

To overcome these limitations, we employ a nonlinear signal decomposition method introduced by Frie and Osorio [21], called the Intrinsic Time scale Decomposition (ITD). ITD allows for the construction of the intrinsic basis functions with finite support, thus allowing for real-time signal decomposition. In the subsequent sections, we show that (a) ITD components effectively capture the key signal features/events, such as singularities (spikes, [22]) as well as changes in the higher-order patterns and intermittencies across multiple decomposition levels, and (b) the detectability of a change may be enhanced by more than 4 times if we combine information from multiple ITD components, thus allowing for a robust change detection approach. Based on these theoretical results, we develop a statistic called InSync for detecting changes in complex dynamical systems. In Section 3, we present numerical simulations and real world case studies to demonstrate the performance of our ITD-based change detection methodology. Finally, we present the concluding remarks in Section 4 with a brief discussion on the performance of proposed change detection method.

2 Overview and properties of ITD

As noted in the forgoing, we employ ITD to decompose a signal into different components, and use phase and amplitude synchronization among a specific set of components to develop a change detection statistic. In this section, we first provide a brief overview of ITD and identify some key properties associated with individual components. We then analyze the behavior of these components at the change points and develop a statistical change detection procedure.

2.1 Intrinsic Time Scale Decomposition

ITD belongs to a general class of Volterra expansions [23] where the signal, $x(t)$ is iteratively decomposed into multiple levels of *rotation components*, $R^j(t), j = 1, 2, ..., J-1$ of progressively decreasing granularity and a global *trend component* $L^J(t)$ as

$$x(t) = \sum_{j=1}^{J-1} R^j(t) + L^J(t) \tag{1}$$

Each $R^j(t)$ satisfies the condition:

$$\left(r_{k+1}^j - r_k^j\right)\left(r_{k+2}^j - r_{k+1}^j\right) < 0$$

where r_k^j are the values of successive extrema of $R^j(t)$ realized at locations τ_k^j(i.e., $r_k^j \equiv R^j(\tau_k^j)), k = 1, 2, \ldots, N^j$ and is monotonic in the interval $(\tau_k^j, \tau_{k+1}^j]$. $R^j(t)$ essentially

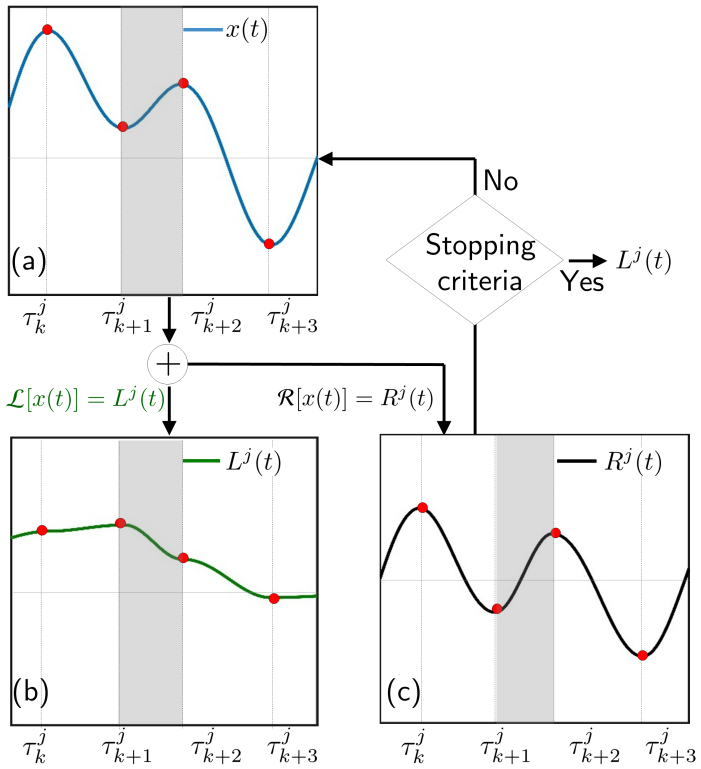

Figure 2: Flow chart showing the recursive decomposition of (a) signal $x(t)$ into (b) the corresponding baseline component $L^j(t)$ (Eq. (3)) and (c) the rotation component $R^j(t)$, Eq. (2). Here, $\mathcal{L}$ and $\mathcal{R}$ are the baseline and residual extracting operators, respectively, such that $\mathcal{L}[L^{j-1}(t)] = L^j(t)$ and $\mathcal{R}[L^{j-1}(t)] = R^j(t)$. Highlighted region shows the support of the intrinsic basis function defined between two consecutive extrema, τ_{k+1}^{j+1} and τ_{k+2}^{j+1}.

captures the "details" of a signal at the decomposition level j. From an algorithm stand point, it is recursively obtained by taking the difference between signal approximations at two consecutive levels, also referred to as *baseline components*, $L^j(t)$, i.e.,

$$R^j(t) = L^{j-1}(t) - L^j(t); \forall j = 1, 2, \ldots, J-1 \tag{2}$$

The baseline component, $L^j(t)$ is defined piecewise between successive extrema $\{\tau_k^j, \tau_{k+1}^j\}$ for all $j = 1, 2, \ldots, J-1$, and is extracted iteratively between the successive extrema as follows (also see Fig. 2(a)):

$$\begin{aligned} L^0(t) &= x(t) \\ L^j(t) &= l_k^j + \left(\frac{l_{k+1}^j - l_k^j}{l_{k+1}^{j-1} - l_k^{j-1}} \right) \left(L^{j-1}(t) - l_k^{j-1} \right) \end{aligned} \tag{3}$$

where $t \in (\tau_k^j, \tau_{k+1}^j]$ and $l_k^j (\equiv L^j(\tau_k^j)), \forall k = 1, 2, ..., N^j$, are the values of successive extrema at the baseline level j. The next extremum, i.e., l_{k+1}^j in Eq. (3) can be obtained recursively as:

$$l_{k+1}^j = \frac{1}{2} \left(l_k^{j-1} + l_{k+1}^{j-1} \right) + \frac{\tau_{k+1}^{j-1} - \tau_k^{j-1}}{\tau_{k+2}^{j-1} - \tau_k^{j-1}} \left(l_{k+2}^{j-1} - l_k^{j-1} \right) \tag{4}$$

As shown in Fig. 2(b), the baseline component, $L^j(t)$ captures the trend of the raw signal $x(t)$ at level j which iteratively forms the basis for decomposition in the next level

and the process continues until the stopping criteria [24] are met. Since ITD performs the decomposition iteratively and recursively between consecutive extrema $(\tau_k^j, \tau_{k+1}^j]$, the intrinsic basis functions, $R^j(t)$ have a finite support (see Fig. 2(c)). Finite support of the basis function allows for a causal representation (assuming a finite number of future points—until the next extremum—is observed), which is essential for change detection. Also, from Eq. (3), we see that the decomposition involves linear operations which can be performed in $\mathcal{O}(cN^0)$ time where, N^0 is the number of extrema in $x(t)$ and $c > 0$.

2.2 Properties of ITD

In this subsection, we first present a half-wave representation of the rotation components and extend a simple construct introduced in [24] to show that the signature of change points have a specific and much higher probability of being retained over multiple decomposition levels j when compared to random signatures.

Property 1. *Each $R^j(t)$ can be represented as a concatenation of halfwaves, $\hbar_k^j(t)$ (see Fig. 3) each of which is defined between two consecutive zero crossings, $\left(z_k^j, z_{k+1}^j\right] \forall k = 1, 2, \ldots, N-1$ as:*

$$R^j(t) = \bigodot_{k=1}^{N-1} \hbar_k^j(t) \tag{5}$$

where each $\hbar_k^j(t)$ has a characteristic amplitude a_k^j and an instantaneous phase component $\phi_k^j(t)$.

Property 2. *Each halfwave, $\hbar_k^j(t)$ is monotonically increasing (decreasing) until the characteristic extrema τ_k^j, and then it decreases (increases) monotonically.*

The halfwaves need not be symmetric or harmonic (i.e., they can be skewed). For example, one can have, $\hbar_k^j(t) \triangleq \left\{R^j(t) | t \in (z_k^j, z_{k+1}^j]\right\}$. In general, $\phi_k^j(t)$ can be determined using the analytic representation of $\hbar_k^j(t)$ given as $\hbar_k^j(t) + i\tilde{\hbar}_k^j(t)$ where $\tilde{\hbar}_k^j(t)$ is the Hilbert Transform of $\hbar_k^j(t)$ such that $\phi_k^j(t) = \tanh(\tilde{\hbar}_k^j(t)/\hbar_k^j(t))$. Frie and Osorio [21] provide additional insights into the calculations of $\phi_k^j(t)$ using linear as well as harmonic halfwave assumptions (see Eq. (19) for piecewise linear phase approximation). Moreover, the halfwave representation allows the definition and extraction of instantaneous phase $\phi_k^j(t)$ and amplitude $a_k^j(t)$ information over a finite support.

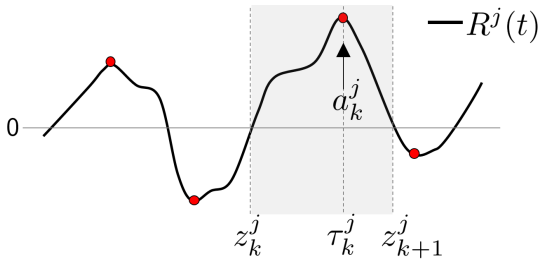

Figure 3: A halfwave, $\hbar_k^j(t)$ defined on $(z_k^j, z_{k+1}^j]$ in $R^j(t)$ such that τ_k^j is the characteristic extrema of $\hbar_k^j(t)$.

Property 3. *It follows from Eqs. (2-4), that $L^j(t)$ and $R^j(t)$ in subsequent levels given the baseline, $L^{j-1}(t)$ depend only on the values of successive extrema points, l_k^j and extrema locations, τ_k^j and not on $L^{j-1}(t)1_{\{t \neq \tau_k^j\}}$ [24].*

We now exploit the aforementioned properties, among others [23,24], to determine the probability with which the information about a change point in level j is retained in the subsequent levels of $R^j(t)$. Towards this end, we construct a time series (with reduced dynamics but without loss of generality [24]; also see Property 3) $x_k = (-1)^k|w_k|; w_k \sim \mathcal{N}(0, \sigma^2), k \in \mathbb{Z}^+$ such that the successive sampled points are alternating maxima and minima. We first present extension of a result from [24] on the probability of retaining an extremum at level j in the subsequent $j + \eta, \eta \in \mathbb{Z}^+$ levels and that it geometrically decays to zero as the value of η increases. Since the successive points in x_k are alternating extrema, the probability of retaining any extremum k^* can be associated with the probability of retaining a (random) feature at k^* in x_k across multiple levels.

Proposition 1. *The probability that an extremum in level j is retained as an extremum in the subsequent η levels is approximately equal to 0.24^η.*

An outline of the proof is presented in Appendix A in the supplemental material. Evident from this result is that the chances of retaining an extremum over three or more decomposition levels decays geometrically fast to 0.

Remark 1. Intuitively, if an extremum in $R^j(t)$ corresponds to a random signature in the parent signal $x(t)$, then the probability that this extremum is retained across subsequent decomposition levels should be very small. In fact, this is in alignment with the previous result where we notice that the probability that an extremum in x_k (white noise) would be retained across two or more subsequent levels ≤ 0.05.

We now extend this result to a more general case by introducing a systemic feature in x_k, such that the baseline component in the first level is represented as:

$$l_k = x_k + \nu\sigma\delta_{k^*} \tag{6}$$

where ν is a non-negative scale variable and δ_{k^*} is Kronecker delta (a variable maximum) given as:

$$\delta_{k^*} = \begin{cases} 1 & k = k^*, \\ 0 & k \neq k^* \end{cases}$$

Here, $\nu\delta_k^*$ is representative of a sharp change point at k^*. Note that with $\nu = 0$, Eq. (6) reduces to x_k. For simplification, each halfwave in l_k is represented by the index k itself, since the successive points in l_k are alternating maxima and minima unless otherwise stated. We now determine the probability, $P_e(\nu)$ of retaining the extremum at k^* as a function of $\nu > 0$ and show that as ν increases, there is a dramatic increase in the value of $P_e(\nu)$. First, we present the following result which is necessary to calculate $P_e(\nu)$:

Proposition 2. *Let r_k^{j+1} be the extrema in the rotation component, $R^{j+1}(t)$ at any decomposition level $j + 1$ of l_k. Then the distribution function of r_k^{j+1}, is given by the convolution of three independent random variables, K_1, K_2 and Γ such that,*

$$F_{r_k^{j+1}}(r) = \int\int\int_{\substack{\{(\kappa_1,\kappa_2,\gamma)\in\mathbb{R}^2\times[0,2\nu\sigma]; \\ \kappa_1+\kappa_2+\gamma\leq r\}}} F_K(d\kappa)F_K(d\kappa)F_\Gamma(d\gamma) \tag{7}$$

where $K_i, i = 1, 2$ are identically distributed and can be represented as a sum of independently distributed normal random variables $l_k^j \sim \boldsymbol{\mathcal{N}}(0, \sigma^2)$ and Θ as:

$$F_K(l, \theta) = \int\limits_{\{(l,\theta)\in\mathbb{R}^2 : l+\theta\leq\kappa\}} \int G_\Theta(d\theta) G_{l_k^j}(dl)$$

where the distribution function of Θ is given as:

$$G_\Theta(\theta) = \int_{-\infty}^{\theta} \left(\int_{\infty}^{\infty} f_{U, l_k^j} \left(l, \frac{\omega}{l} \frac{1}{|l|} dl \right) d\omega \right)$$

with $U \sim uniform(0, 2)$ and $l_k^j \sim \boldsymbol{\mathcal{N}}(0, \sigma^2)$. Γ follows a mixture distribution such that:

$$F_\Gamma(\gamma) = \int_0^\gamma \frac{1}{2\nu\sigma} d\omega 1_{k=k^*\pm 1} + c 1_{k=k^*}$$

where $c > 0$.

Before we prove the above result, we first present two necessary lemmas:

Lemma 1. *Let the inter-extremal separations be defined as $\Delta_k^j := \left(\tau_k^j - \tau_{k-1}^j\right)$. With proper continuity conditions, Δ_k^j follows an exponential distribution as*

$$F(\Delta_k^j) = 1 - \exp\left(\Delta_k^j / \lambda^j\right)$$

where $\lambda^j = \mathbb{E}[\Delta_k^j]$.

Lemma 2. *Let q_k^j be defined as follows:*

$$q_k^j := \frac{(\tau_k^j - \tau_{k-1}^j) - (\tau_{k+1}^j - \tau_k^j)}{(\tau_k^j - \tau_{k-1}^j) + (\tau_{k+1}^j - \tau_k^j)} = \frac{\Delta_k^j - \Delta_{k+1}^j}{\Delta_k^j + \Delta_{k+1}^j} \tag{8}$$

Then $q_k^j \ \forall k = 1, 2, \ldots, N; j \in J$, follows a uniform(-1,1) distribution.

See Appendix B in the supplemental material for the proof of the above two lemmas. We now present the proof of Proposition 2 as follows:

Proof. Using the compact notation introduced in [24], we can represent the extrema vector, $\boldsymbol{l}^{j+1} = [l_k^{j+1}]_{k=1,2,\ldots,N}$ in the baseline component at level $j+1$ as:

$$\boldsymbol{l}^{j+1} = \boldsymbol{\mathcal{T}}\left(\tilde{\boldsymbol{l}}^{j+1}\right) \tag{9}$$

where $\boldsymbol{\mathcal{T}}$ is an extrema extracting operator such that $\tilde{\boldsymbol{l}}^{j+1} = (I + M^j)\, \boldsymbol{l}^j$ and M^j is the tri-diagonal matrix as follows:

$$M^j = \begin{pmatrix} 2 & 2 & 0 & \ldots & 0 \\ 1 - q_2^j & 2 & 1 + q_2^j & \ldots & 0 \\ 0 & 1 - q_3^j & 2 & \ddots & \vdots \\ 0 & 0 & 0 & \ldots & 2 \end{pmatrix}; \boldsymbol{l}^j = \begin{pmatrix} l_1^j \\ l_2^j \\ \vdots \\ l_N^j \end{pmatrix}$$

Thus, Eq. (9) can be rewritten as:

$$\boldsymbol{l}^{j+1} = \boldsymbol{\mathcal{T}}\left[(I+M^j)\boldsymbol{l}^j + \nu\sigma(I+M^j)e_{k^*}\right] = \boldsymbol{\mathcal{T}}\left[\left(I+M^j\right)\boldsymbol{l}^j + \frac{1}{4}\begin{bmatrix} \underline{0} \\ (1+q^j_{k^*-1})\nu\sigma \\ 2\nu\sigma \\ (1-q^j_{k^*+1})\nu\sigma \\ \underline{0} \end{bmatrix}\right] \quad (10)$$

where $e_{k^*} = \begin{bmatrix}\underline{0} & 1_{\{k=k^*\}} & \underline{0}\end{bmatrix}^T$. Consequently the "$\nu\sigma$" containing terms in Eq. (10) are:

$$\begin{bmatrix} \tilde{l}^{j+1}_{k^*-1} \\ \tilde{l}^{j+1}_{k^*} \\ \tilde{l}^{j+1}_{k^*+1} \end{bmatrix} = \frac{1}{4}\begin{bmatrix} q^{j-}_{k^*-1}l^j_{k^*-2} + 2l^j_{k^*-1} + q^{j+}_{k^*-1}l^j_{k^*} + q^{j+}_{k^*-1}\nu\sigma \\ q^{j-}_{k^*}l^j_{k^*-1} + 2l^j_{k^*} + q^{j+}_{k^*}l^j_{k^*+1} + 2\nu\sigma \\ q^{j-}_{k^*+1}l^j_{k^*} + 2l^j_{k^*+1} + q^{j+}_{k^*+1}l^j_{k^*+2} + q^{j-}_{k^*+1}\nu\sigma \end{bmatrix}$$

where, $q^{j-}_k = 1 - q^j_k$ and $q^{j+}_k = 1 + q^j_k$. Notice that without the operator $\boldsymbol{\mathcal{T}}$ in Eq. (10), terms on the LHS may not be guaranteed to be extrema (see Property 1 in supplemental material). The corresponding points in the rotation components are given as follows:

$$\tilde{r}^{j+1}_k = \begin{cases} \frac{1}{4}\left\{\left(2l^j_k - q^{j-}_k l^j_{k-1} - q^{j+}_k l^j_{k+1}\right)\right\}, & k^*-1 > k > k^*+1 \\ \frac{1}{4}\left\{\left(2l^j_k - q^{j-}_k l^j_{k-1} - q^{j+}_k l^j_{k+1}\right)\right\} + f_k, & k^*-1 \le k \le k^*+1 \end{cases} \quad (11)$$

Again, $\{\tilde{r}^{j+1}_k\}_{k=1,2,\ldots,N}$ represent only the corresponding values of r^j_k in level $j+1$ and not the extrema points. f_k in Eq. (11) represents the the effect of scaled Kronecker delta $\nu\sigma\delta_{k^*}$ (at k^* in level j) at locations k^*-1, k^* and k^*+1 in level $j+1$ such that:

$$f_k = \begin{cases} \nu\sigma/2 & k = k^* \\ -q^{j\mp}_{k^*\mp1}\nu\sigma/4 & k = k^* \mp 1 \\ 0 & \text{o.w.} \end{cases} \quad (12)$$

Therefore, $1+q^j_{k^*}$ and $1-q^j_{k^*}$ follows uniform$(0,2)$ distribution. Let us define, $\Theta := \left(1 \pm q^j_k\right) l^j_{k+1}$ with distribution function G_Θ where $l^j_{k^*+1} \sim N(0,\sigma^2)$. Therefore, G_Θ is the product distribution given as follows:

$$G_\Theta(\theta) = \int_{-\infty}^{\theta}\left(\int_{\infty}^{\infty} f_{U,l^j_k}\left(l, \frac{\omega}{l}\frac{1}{|l|}dl\right)d\omega\right)$$

Next, we define $K_1 := l^j_k - (1-q^j_{k+1})l^j_{k-1}$, which is the sum of normal random variable, $l^j_k \sim G_{l^j_k}(l)$ and $\Theta \sim G_\Theta(\theta)$. Similarly, we define, $K_2 := l^j_k - (1+q^j_{k-1})l^j_{k-1}$ such that:

$$F_K(l,\theta) = \int\int_{\{(l,\theta)\in\mathbb{R}^2 : l+\theta\le\kappa\}} G_\Theta(d\theta)G_{l^j_k}(dl)$$

Now, from Eq. (11), we have $r^{j+1}_k \left(= \boldsymbol{\mathcal{T}}[\tilde{r}^{j+1}_k]\right)$ as the sum of K_1, K_2 and $\Gamma\,(= f_k)$. Also, from the definition of Γ in Eq. (12), we have K_1, K_2 and Γ are independently distributed where Γ is a mixture distribution given as

$$F_\Gamma(\gamma) = \int_0^\gamma \frac{1}{4\nu\sigma}d\omega 1_{t=\tau^j_{k^*\pm1}} + \frac{\nu\sigma}{2}1_{t=\tau^j_{k^*}}$$

Combining the above results, we have

$$F_{r_k^{j+1}}(r) = \int\int\int_{\substack{\{(\kappa_1,\kappa_2,\gamma)\in\mathbb{R}^2\times[0,2\nu\sigma];\\ \kappa_1+\kappa_2+\gamma\leq r\}}} F_K(d\kappa)F_K(d\kappa)F_\Gamma(d\gamma) \qquad \square$$

Now, for $r_{k^*}^{j+1}$ to be a maximum given that $r_{k^*}^{j}$ is a maximum (with probability 1), we need $r_{k^*}^{j+1} - r_{k^*-1}^{j+1} > 0$ and $r_{k^*}^{j+1} - r_{k^*+1}^{j+1} > 0$ simultaneously. Therefore, the probability that $r_{k^*}^{j}$ is retained as a maximum in level $j+1$ is given as:

$$P_e(\nu) = P\left(r_{k^*}^{j+1} - r_{k^*-1}^{j+1} > 0\right) P\left(r_{k^*}^{j+1} - r_{k^*+1}^{j+1} > 0\right) \tag{13}$$

To simplify subsequent analysis, we present the following result:

Corollary 1. *The probability $P_e(\nu)$ in Eq. (13), with first order Gaussian approximations to the distribution function to r_k^{j+1}, can be deduced in closed form as:*

$$\hat{P}_e(\nu) = \left[1 - P\left(\mathcal{Z} \leq -\frac{\nu}{\sqrt{2}}\right)\right]^2 \tag{14}$$

where $\mathcal{Z} \sim N(0,1)$.

Proof of the corollary is presented in Appendix C in the supplemental material. We validate the values of $P_e(\nu)$ and $\hat{P}_e(\nu)$ obtained from Eqs. (13 & S9), respectively, against the empirical distribution estimated from multiple realizations of l_k^j. We use Monte Carlo (MC) simulation to estimate $P_e(\nu)$. From Fig. 4(a), we notice that the MC simulation of $P_e(\nu)$ as well as the Gaussian approximation, $\hat{P}_e(\nu)$ closely capture the actual simulation results (Eq. (3)). For $\nu = 0$, $P_e(0)(= 0.25)$ simply is the probability that a maximum in level $R^j(t)$ is retained as a maximum in $R^{j+1}(t)$ and is also consistent with the result stated in Proposition 1.

Remark 2. From Fig. 4(a), we notice that the probability of retaining a systemic feature at k^* in the two subsequent levels for $\nu \geq 3$ is greater than 0.9, unlike $P_e(0)$, which geometrically decays to below 0.05 as noted in Remark 1. This suggests that the information about this systemic feature is preserved across multiple levels.

Following from Fig. 4(a), the sharp rise in $P_e(\nu)$ can be explained from the Gaussian approximation of r_k^{j+1} where (see proof of Corollary 1, Appendix C),

$$\left(\hat{r}_{k^*}^{j+1} - \hat{r}_{k^*\pm1}^{j+1}\right) \sim \boldsymbol{\mathcal{N}}\left(\frac{\nu}{4}, \frac{1}{8}\right)$$

Therefore, as ν increases, the mean of $\left(\hat{r}_{k^*}^{j+1} - \hat{r}_{k^*\pm1}^{j+1}\right)$ shifts linearly on the positive ν axis resulting in a steep increase in $P_e(\nu)$. The above results establish the probabilities with which key features at some level $R^j(t)$ may be retained across subsequent levels. These results are significant from a change detection standpoint because the key features at the change points, such as singularities need to be retained over multiple levels in order to enhance their detectability.

Next considered that the systemic feature introduced in Proposition 2 at $k = k^*$ be defined as a singularity iff $r_{k^*}^{j} \geq 3\sigma^j$, then the lower bound on the conditional probability,

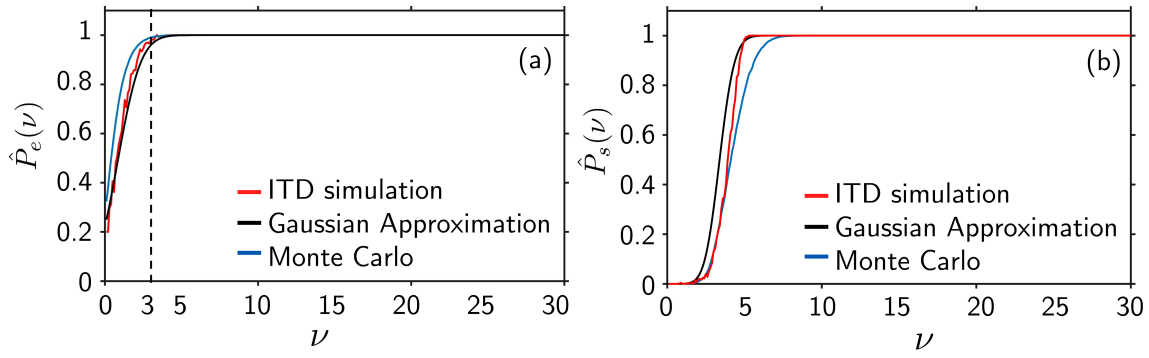

Figure 4: Comparison of (a) the probabilities that a maximum at k^* in level j is retained as a maximum in level $j+1$ obtained from Eqs. (13 & S9), i.e., $P_e(\nu)$ and $\hat{P}_e(\nu)$, respectively and (b) shows the conditional probabilities, that a singularity at level j is retained as a singularity in level $j+1$ obtained from Eqs. (15 & 16), i.e., $P_s(\nu)$ and $\hat{P}_s(\nu)$, respectively, against the empirical evidence obtained via the simulation of l_k^j (see Eq. (3)).

$P_s(\nu)$ that a singularity in level j remains as a singularity in level $j+1$ can be defined as,

$$P_s(\nu) := P\left(r_{k^*}^{j+1} > 3\sigma^{j+1} \middle| \nu \geq 3\sigma^j\right) \tag{15}$$

Corollary 2. *Using the Gaussian approximation to r_k^{j+1} (see Appendix C), $P_s(\nu)$ can be approximated as,*

$$\hat{P}_s(\nu) = 1 - P\left(\mathcal{Z} \leq 3 - \nu\sqrt{19/16}\right) \tag{16}$$

Proof of the corollary is given in Appendix D in the supplemental material. Results from MC simulation of $P_s(\nu)$ (Eq. (15)) and the corresponding Gaussian approximation, $\hat{P}_s(\nu)$ (Eq. 16)) are compared against the empirical results of Eq. (3). We notice from Fig. 4(b), that both $P_s(\nu)$ and $\hat{P}_s(\nu)$ are consistent with the empirical trend. More pertinently, we note that the conditional probability of retaining the singularity across subsequent levels is close to 1 for $\nu > 3$. Again, the steep increase in $\hat{P}_s(\nu)$ in Fig. 4(b) can be understood from the Gaussian approximation of $r_{k^*}^{j+1}$. Since $r_{k^*}^{j+1} \sim \mathcal{N}\left(\frac{\nu}{4}, \frac{1}{19}\right)$, for $\frac{\nu}{4} + 3\sqrt{\frac{1}{19}} \leq 3\sigma^j$, $P_s(\nu)$ remains close to 0 and then increases steeply when the above condition no longer holds. This is because the mean of $r_{k^*}^{j+1}$ increases linearly as a function of ν with variance $\ll 1$. More interestingly, $\nu = 3\sigma$ acts as an activation barrier such that $\hat{P}_s(\nu) \to 1$ as $\nu > 3\sigma$. Moreover, since Fig. 4(b) presents a lower limit on $\hat{P}_s(\nu)$, hence a singularity in level j may be preserved with much higher probability in the subsequent rotation components than that reported in Eq. (16).

3 Intrinsic Phase Synchronization

Now, we know that the probability with which a singularity (and other sharp features) is retained across multiple levels of $R^j(t)$ is significantly higher than some random signal patterns. Thus, combining information from multiple levels can significantly enhance the specificity of detecting these sharp features. We next employ phase synchronization concepts to determine and combine the amount of information that is contained over multiple levels of $\{R^j(t)\}_{j\in J}$ as follows:

Definition 1. Phase synchronization between a halfwave $\hbar_k^{j_1}(t)$ of $R^{j_1}(t)$ and the fraction of corresponding halfwave $\hbar_k^{j_2}(t)$ at level $j_2 > j_1$, within $supp\left(\hbar_k^{j_1}(t)\right) = (z_k^j, z_{k+1}^j]$ is defined as:

$$\Phi_k^{j_1,j_2} = \frac{\left\langle \phi_k^{j_1}(t), \phi_k^{j_2}(t) \right\rangle}{\left\| \phi_k^{j_1}(t) \right\| \left\| \phi_k^{j_2}(t) \right\|} \tag{17}$$

Th aforementioned definition of phase synchronization is an improvement over the classical definition of phase synchronization ($|\phi_k^{j_1}(t) - \phi_k^{j_2}(t)|$, [15]), in that, it is more robust to slight variations in the phases resulting due to noise effects and provides a direct measure to quantify the strength of synchronization between halfwaves at different levels. Comparatively, the classical approach only provides an indirect quantification with expected value of $|\phi_k^{j_1}(t) - \phi_k^{j_2}(t)| \to 0$ for highly synchronized halfwaves. Additionally, with this definition, we can estimate the increase in the expected level of phase synchronization when there is a singularity (change point) versus no singularity. This is captured in the following proposition:

Proposition 3. *Whenever a singularity is present at $k = k^*$ in level j and $P_s(\nu)$ is the probability that this singularity is retained as a singularity in level $j+1$, we have,*

$$\xi = \frac{E\left[\Phi_k^{j,j+1} \middle| r_{k^*}^j \geq 3\sigma^j\right]}{E\left[\Phi_k^{j,j+1} \middle| r_{k^*}^j < 3\sigma^j\right]} \tag{18}$$

such that ξ is lower bounded as,

$$\xi \geq P_s(\nu|\nu > 3\sigma^j) \lim_{h\to 0}(P_e(h))^{-1} = 4P_s(\nu|\nu > 3\sigma^j)$$

Proof. In order to determine the expected level of phase synchronization between halfwave at levels j and $j+1$, $\Phi_k^{j,j+1}$, we first identify the fraction of halfwave, $\hbar_k^{j+1}(t)$ enclosed within the support, $\text{supp}(\hbar_k^j)$. This is represented by the shaded region in Fig. 5(a). Assuming that the extrema, τ_k^j at level j is retained in the next level, then its neighboring extrema may evolve in the next level according to either extrema vanishing or extrema preserving transition (see Property 1 in the supplemental material). Here, $\text{supp}(\hbar_k^{j+1}) = (z_k, z_{k+1}]$ where z_k^{j+1} and z_{k+1}^{j+1} are variables and depend on the location of $r_{k^{\pm 1}}^{j+1}$ (This may not be guaranteed to be an extremum in level $j+1$, see Eq. (10). Under the given assumptions, some possible cases for the evolution of τ_{k-1}^j and τ_{k+1}^j in level $j+1$ are as shown in Fig. 5(b). These are, (i) all the extrema, τ_k^j and $\tau_{k\pm 1}^j$ being preserved, (ii) only the minimum at τ_{k-1}^j vanishes, hence shifting z_k^{j+1} towards left, (iii) minimum at τ_{k+1}^j vanishes causing z_{k+1}^j to shift towards right, (iv) similarly if minima on either side of τ_k^j vanishes, increasing the support of $\hbar_k^j$ on both the directions, and so on.

First consider the halfwave, $\hbar_k^j(t)$ to be characterized by points $\{R^j(z_k^j), r_k^j, R^j(z_{k+1}^j)\} \equiv \{0, r_k^j, 0\}$. Similarly, the points $\{R^{j+1}(z_k^j), r_k^{j+1}, R^{j+1}(z_{k+1}^j)\}$ defines the corresponding halfwave in the next level, i.e., $\hbar_k^{j+1}(t)$ enclosed within $(z_k, z_{k+1}]$. Here, $R^{j+1}(z_k^j)$ and $R^{j+1}(z_{k+1}^j)$ are the amplitudes of $R^j(z_k^j)$ and $R^j(z_{k+1}^j)$, i.e., the amplitudes of zero crossings z_k^j and z_{k+1}^j in level $j+1$. We use linear interpolation to determine the values of $R^{j+1}(z_k^j)$ and $R^{j+1}(z_{k+1}^j)$ as follows:

$$R^{j+1}(z_k^j) = r_{k-1}^{j+1} + \frac{R^{j+1}(\tau_k^j) - R^{j+1}(\tau_{k-1}^j)}{\tau_k^j - \tau_{k-1}^j}\left(z_k^j - \tau_{k-1}^j\right)$$

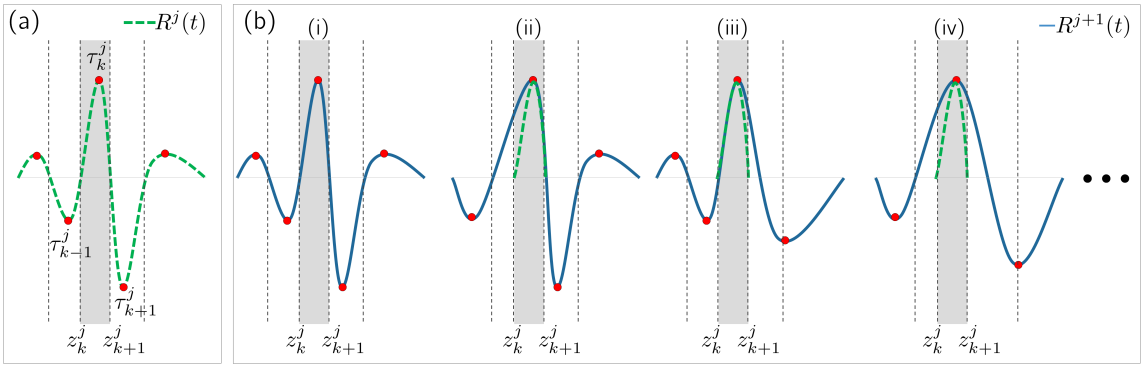

Figure 5: (a) A representative halfwave, $\hbar_k^j(t)$ in level j with characteristic extrema at τ_k^j, (b) shows the few possible cases in which extrema in level j at τ_k^j shown in (a) may evolve in level $j+1$.

and

$$R^{j+1}(z_{k+1}^j) = r_k^{j+1} - \frac{R^{j+1}(\tau_k^j) - R^{j+1}(\tau_{k+1}^j)}{\tau_{k+1}^j - \tau_k^j}\left(z_{k+1}^j - \tau_k^j\right)$$

Since phase is invariant of translation, $\hbar_k^{j+1}(t)$ can be translated and equivalently represented by the points $\{0, r_k^{j+1} - R^{j+1}(z_k^j), R^{j+1}(z_{k+1}^j) - R^{j+1}(z_k^j)\}$. To determine the expected phase synchronization, it would suffice to determine the inner product between the instantaneous phase of halfwaves $\hbar_k^j$ and $\hbar_k^{j+1}$ within the support of $\hbar_k^j$. Extracting the instantaneous phase for each of the halfwaves using Hilbert transform may not be optimal since it is not causal and may cause phase distortion at the edges. To overcome these issues, we use a piece-wise linear phase introduced in [21] as:

$$\phi_k^j(t) = \begin{cases} \sin^{-1}\left(\dfrac{R^j(t)}{r_k^j}\right), & t \in [z_k^j, \tau_k^j] \\ \pi - \sin^{-1}\left(\dfrac{R^j(t)}{r_k^j}\right), & t \in [\tau_k^j, z_{k+1}^j] \end{cases} \tag{19}$$

Therefore, expected level of phase synchronization can be calculated by individually by determining the phase synchronization values on each half, i.e., on the support, $[z_{k-1}^j, \tau_k^j]$ and $[\tau_k^j, z_k^j]$. Considering singularity at k, this can be represented as follows:

$$\mathbb{E}\left[\Phi_{k^*}^{j,j+1} | \nu \geq \nu_0\right] = P_s(\nu)\,(I + II)$$

where,

$$I = \frac{\int_{z_{k^*}^j}^{\tau_{k^*}^j} \phi_{k^*}^j(t)\phi_{k^*}^{j+1}(t)dt}{\left(\sqrt{||\phi_{k^*}^j(t)|| \times ||\phi_{k^*}^j(t)||}\right)\Big|_{\{z_{k^*}^j < t < \tau_{k^*}^j\}}}$$

and

$$II = \frac{\int_{\tau_{k^*}^j}^{z_{k^*+1}^j} \phi_{k^*}^j(t)\phi_{k^*}^{j+1}(t)dt}{\left(\sqrt{||\phi_{k^*}^j(t)|| \times ||\phi_{k^*}^j(t)||}\right)\Big|_{\{\tau_{k^*}^j < t < z_{k^*+1}^j\}}}$$

Clearly, the first term is equal to 1 since the phase is invariant to halfwave scaling (see the 3-point representation of halfwaves) and let the second term be equal to $1-\delta$ where δ is the deviation from perfect synchronization and is proportional to $R^{j+1}(z^j_{k^*}) - R^{j+1}(z^j_{k^*-1})$ which is equal to: $\frac{1}{2}\big(R^{j+1}(\tau^j_{k^*+1}) - R^{j+1}(\tau^j_{k^*-1})\big)$ which is approximately normally distributed with mean and standard deviation function of ν. However, phase is invariant to scaling, hence the value of II is independent of ν. For the case when $\tau^j_{k^*}$ is not a singularity, the probability of observing transitions as shown in Fig. 5(b) is equal to the probability of retaining the extremum at $\tau^j_{k^*}$ as an extremum in level $j+1$. So, we can write the expected phase synchronization for this case as the following sum,

$$\mathbb{E}\left[\Phi^{j,j+1}_{k^*} | r^j_{k^*} < 3\sigma^j\right] = P_e(\nu|\nu=0)P(\mathcal{Z} < 3\sigma^j)\Big[I + II\Big] + \eta_1 + \eta_2$$

where η_1 and η_2 are the expected phase synchronization when the extremum at $\tau^j_{k^*}$ vanishes and when the extremum flips in sign respectively. Here, η_2 is negative since the halfwave at level j would be negatively oriented with respect to $\hbar^j_{k^*}$. The term $\eta_1 \approx 0$ because the halfwaves at level j and $j+1$ would be approximately orthogonal since the halfwave $\hbar^j_{k^*}$ is convex while $\hbar^{j+1}_{k^*}$ would be linear. Hence, we have,

$$\mathbb{E}\left[\Phi^{j,j+1}_{k^*} | r^j_{k^*} < 3\sigma^j\right] \leq P_e(\nu|\nu=0)P(\mathcal{Z} < 3\sigma^j)\Big[I + II]$$

Therefore, the ratio of expected level of phase synchronization between the halfwaves, $\hbar^j_{k^*}$ at level j and $j+1$ when $\tau^j_{k^*}$ is a singularity to when it is not a singularity, given that the extremum at $\tau^j_{k^*}$ is retained as an extremum is given as,

$$\begin{aligned}
\xi &= \frac{\mathbb{E}\left[\Phi^{j,j+1}_{k^*} | r^j_{k^*} \geq 3\sigma^j\right]}{P_e(\nu|\nu=0)\mathbb{E}\left[\Phi^{j,j+1}_{k^*} | r^j_{k^*} < 3\sigma^j\right]} \\
&\geq \frac{\mathbb{E}\left[\Phi^{j,j+1}_{k^*} | \nu \geq 3\sigma^j\right]}{P_e(\nu|\nu=0)\mathbb{E}\left[\Phi^{j,j+1}_{k^*} | r^j_{k^*} < 3\sigma^j\right]} \\
&\geq \frac{P_s(\nu|\nu \geq 3\sigma^j)[I + II]}{P_e(\nu|\nu=0)P(\mathcal{Z} < 3\sigma^j)[I + II]}
\end{aligned}$$

On simplification, we get,

$$\xi \geq \frac{P_s(\nu|\nu > 3\sigma^j)}{P_e(\nu|\nu=0)P(\mathcal{Z} < 3\sigma^j)} \approx 4P_s(\nu|\nu > 3\sigma^j) \qquad \square$$

Here, we note that as $P_s(\nu) \to 1$, we have $\xi \geq 4$. This implies that whenever there is a singularity in $R^j(t)$, expected level of phase synchronization between the corresponding halfwaves at level j and $j+1$ will be amplified by more than 4 folds as compared to when there is no singularity. It also suggests that information about a singularity is reflected in the phase synchronization statistic among the corresponding halfwaves.

Our experimental observations, consistent with an earlier result reported in [25] suggest that dynamical systems where change points are characterized by second/higher order moment shift in nonlinear, nonstationary systems, exhibits a high level of Amplitude Envelope Synchronization (AES) (synchronization between the envelopes of maxima

and minima at two different levels of ITD components rather than the components themselves; see [26] for more discussion) among a set of rotation components, $\{R^j(t)\}_{j\in J}$. Therefore, the expected level of AES among the components that would capture the most variations in the amplitude component would be higher compared to the remaining components.

3.1 Maximal Mutual Agreement

As seen in the foregoing, information (both phase and amplitude) about any change is preserved across multiple ITD components. Therefore, it is important to select a set of rotation components that would be dynamically similar so that the information contained therein, when fused together, would be positively reinforced resulting in an enhanced sensitivity and specificity about the change points. To address this point, we introduce the concept of ***maximal mutual agreement*** as follows:

Definition 2. A set of rotation components, $\mathcal{G}$, with maximal mutual agreement is the minimal set of $\{R^j(t)\}_{j\in J}$ that would capture and reinforce the information about a key feature or change.

In order to determine $\mathcal{G}$ we employ a graph representation G of the intrinsic components of $x(t)$ such that, $G = (V, E)$ where $V = \{R^j(t)\}_{j\in J}$ and $E = (m(R^i(t), R^j(t)))_{i,j\in J, i\neq j}$, with $m(.,.)$ as the maximal information coefficient [27] based on the mutual information function between $R^i(t)$ and $R^j(t)$. We use the weighted degree centrality of each node, $\mathcal{M}^j = \sum_{i\neq j} m(R^i(t), R^j(t))$, as a measure of mutual agreement between $R^j(t)$ and $\{R^i(t)\}_{i\neq j}$. It is shown in [28] that $\mathcal{M}^j$ effectively captures the dynamical synchronization between the network elements. Here we deem the rotation components, $R^j(t)$ for which M^j is greater than a specified Pareto threshold, ϑ_p [29] constitute the set $\mathcal{G}$.

An illustrative example of the method is shown in Fig. 6. Here, the arc thickness and the node size are scaled according to the magnitude of $m(R^i, R^j)\forall i, j = 1, 2, \ldots, J; i \neq j$ and $\mathcal{M}^j$, respectively. We notice from Fig. 6(a) that the $\mathcal{M}^j$ values of the rotation components $R^1(t), R^5(t), R^6(t), R^7(t)$ and $R^8(t)$ are less than the Pareto threshold shown in Fig. 6(b) and hence can be discarded. Therefore, the set of rotation components with maximal mutual agreement would be, $\mathcal{G} = \{R^2(t), R^3(t), R^4(t)\}$. For multiple change points in the signal, clusters of rotation components with significant $\mathcal{M}^j$ values, each capturing the respective type of change point may be observed. For a sufficiently long time series, changes such as singularities (small-scale features) are mostly captured by lower level rotation components (typically $j \leq 3$ as shown in the previous example) while gradual changes such as trend or second order moment shifts are generally captured by higher level components (typically $j > 3$). Constructing the network locally in time, rather than for the complete time series would help in identifying different change points from different clusters of rotation components.

3.2 The InSync statistic

In this section, we develop a statistic that would capture and fuse the local phase and amplitude information contained across the set of rotation components with maximal mutual information. Before that, we invoke another property of rotation components that would allow us to combine the phase and amplitude information from the rotation components with maximal mutual agreement.

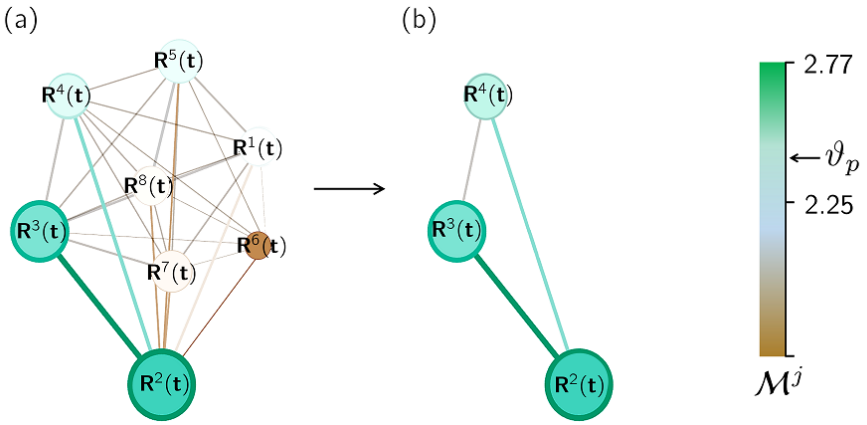

Figure 6: Network representation of the rotation components, $\{R^j(t)\}$ where the edge weight of the arc connecting a node pair (i.e., $R^j(t)$ and $R^f(t)$) is defined by the maximal mutual information, $m(R^f(t), R^j(t))$. By using an appropriate Pareto threshold (ϑ_p), we select the components with maximal mutual agreement.

Proposition 4 (Property 4). *The support of $\hbar_k^j(t)$ at any level $j \geq 2$ spans at least one halfwave $\hbar_k^i(t)$ from its sub-level $\{R^i(t)\}_{i<j}$ and at most one $\hbar_k^f(t)$ from its super-level $\{R^f(t)\}_{f>j}$ as shown in Fig. 7.*

Proof of this proposition is presented in Appendix E in the supplemental material. This property of ITD components, $R^j(t)$ allows us to quantify and fuse the phase and amplitude information contained in the halfwaves across multiple levels within the support of a base halfwave. This forms the basis for development of the InSync statistic which inherently utilizes the Kolmogorov's energy cascading principle to combine the phase and amplitude information across multiple levels [30]. First, we select a base (or reference) rotation component, $R^b(t)$ such that it satisfies, $R^b(t) = \left\{R^j(t) \middle| \mathcal{M}^j = max\left\{\mathcal{M}^1, \mathcal{M}^2, \ldots, \mathcal{M}^J\right\}\right\}$. Based this base component $R^b(t)$, we define the InSync statistic as:

$$\mathcal{I}\left(\hbar_k^b(t)\right) = \left(\sum_{j\in\mathcal{F}} g\left[\mathcal{E}(\hbar_k^j(t))\right]\right) \times \prod_{j\in\mathcal{F}} \Phi_k^{b,j} \tag{20}$$

such that for each halfwave(s) $\hbar_k^j(t)$, $t \in \text{supp}(\hbar_k^b(t))$ where $\hbar_k^b(t)$ is a base halfwave. Here $g(x) = e^{\alpha x}; \alpha > 0$ is a contrast enhancement function with scale factor α and $\mathcal{E}(.)$ is the energy extracting operator for each of the halfwave, $\hbar_k^j(t)$. The first term is the energy (or amplitude) component extracted from the base level halfwaves, $\hbar_k^b(t)$, superimposed with the energy levels of halfwaves at sub ($j < b$) and super ($j > b$) levels of $R^j(t)$. Here, the amplitude term in $\mathcal{I}\left(\hbar_k^b(t)\right)$ is derived from the energy cascading principle, where energy is transferred from larger eddies (ocean currents) to smaller scale eddies as introduced by Kolmogorov and a similar inverse energy cascade principle [30]. The superimposed energy component is then fused with the phase synchronization among the corresponding components. Notionally, InSync is analogous to the energy-based statistics employed in multi-scale analysis methods for change detection fused the intrinsic phase synchronization component. However, with an additional phase synchronization component, the statistic can capture the dynamic as well as sharp change-related information contained in various signal components more effectively compared to other contemporary methods, as can be gathered from various case studies presented in the following section.

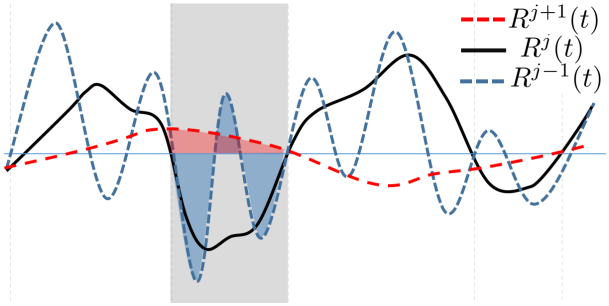

Figure 7: Illustrative example to show the halfwave span property of the rotation components, $R^j(t)$. We notice that the support of $\hbar_k^j(t)$, i.e., $(z_k^j, z_{k+1}^j]$ in $R^j(t)$ spans 3 halfwaves from the previous level, $R^{j-1}(t)$ and a fraction of halfwave from the next level rotation component, $R^{j+1}(t)$.

4 Case Studies

4.0.1 Experimental setup

We investigated the ability of the InSync statistic to detect changes in nonlinear and nonstationary systems using two carefully designed numerical simulations as well as using industrial and neurophysiological time-series signals from real-world settings. We compared the performance of our method with those resulting from the use of conventional approaches, mainly Exponentially Weighted Moving Average (EWMA) and rather contemporary methods including, Standard Deviation-Wavelet based CUSUM (SD-WCUSUM) method [31], traditional recurrence plots (RP) [32] and other problem specific approaches. Direct application of these methods on the time series either did not capture the change points under nonstationary conditions or were found to be ineffective under the presence of noise. We employed the average run length (ARL1 = 1/sensitivity) to compare the sensitivity of each method with ARL0 = 0.0027. ARL1 values were calculated from the CUSUM chart of the InSync statistic. We generated 100 replications of the time-series in numerical simulations to develop a consistent estimate of ARL1.

4.0.2 Recurrence plot based change point visualization

Along with the ARL1 values, we also employed recurrence plots (RP) to visualize the change points. RP is a non-linear time series analysis tool which provides a two dimensional representation, $[\mathbb{D}]_{ij} = ||x^m(t_i) - x^m(t_j)||; i, j \in n$, of the evolution of its trajectory in the phase space. Here, $x^m(t_i)$ is the realization of the trajectory at time t_i when embedded in an m-dimensional phase space such that:

$$x^m(t_i) = \big(x(t_i), x(t_{i+d}), x(t_{i+2d}, ..., x(t_{i+(m-1)d}))\big) \tag{21}$$

where m and d are the optimal embedding dimension and time delay [33]. Due to Taken (Taken's theorem, [33]), $x^m(t_i)$ are $x(t)$ are diffeomorphisms, hence representing the same dynamical system, but in different co-ordinate systems

From a change detection perspective, values of $D_{ij} \to 0$ suggests that the state of the system recurs at the corresponding times, representing a slowing evolving system. In contrast to which, increasing values of D_{ij} suggests that the system shows abrupt bursts or drift in its state with respect to any given time point, t_i, hence capturing different change points.

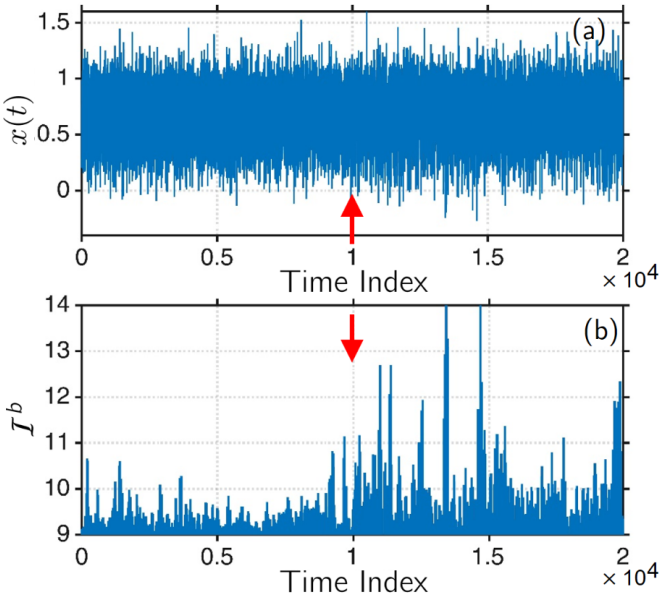

Figure 8: (a) Time series of logistic map, $x(t)$ with SNR= 10 where the change point in the system is indicated by arrow at 10000; (b) shows the InSync statistic $\mathcal{I}(\hbar_k^4(t))$ with the set $\mathcal{G}$ being $\{R^3(t), R^4(t), R^5(t)\}$.

4.1 Dynamic regime change in logistic map

To test the performance of our method for detecting changes between two nonlinear regimes, we generated a 20000 data points long time-series, $x(t)$ from the following logistic map model, superimposed with Gaussian noise:

$$\begin{aligned} x(t) &= y(t) + N(0, \sigma) \\ y(t+1) &= \mu y(t)(1 - y(t)); \mu > 0, t \in \mathbb{Z}^+ \end{aligned} \tag{22}$$

The value of signal to noise ratio (SNR) is varied from 5 to 20 by changing the values of σ in Eq. (22) where SNR is calculated as SNR $= P_{\text{signal}}/P_{\text{noise}}$. A typical realization of $x(t)$ with SNR= 10 is shown in Fig. 8(a).

To introduce a dynamical change, the value of μ is changed from 3.4 (periodic regime) to 3.7 (chaotic regime) at $t = 10000$ time units (t.u.) as shown in Fig. 8(a). Evidently, this change is not discernible from the direct examination of the time portrait. To implement the proposed methodology, we first determined the base component, $R^b(t)$ from the network representation as shown in section 3.1. Here $R^4(t)$ has the maximum value of $\mathcal{M}^j$, hence we selected this as the base component and the corresponding set of components with maximal mutual agreement include, $\mathcal{G} = \{R^3(t), R^4(t), R^5(t)\}$. For the set $\mathcal{G}$, we calculated the InSync statistic, $\mathcal{I}(\hbar_k^4(t))$ for every halfwave defined about the base level $j = 4$. This is shown in Fig. 8(b). One can note a discernible contrast in the values of the statistic between the two dynamic regimes. To compare the performance of the proposed method, we compared the ARL1 values from EWMA and SD-WCUSUM for different values of SNR. This is shown in Table 1. We notice that in all the cases, InSync statistic was able to consistently detect the change point with ARL1 value which is almost two orders of magnitude smaller as compared to EWMA or SD-WCUSUM. We also gathered insights into the contrast enhancement capability of the InSync statistic in detecting changes by using the RP which can effectively capture the variation in a given dynamical system when embedded into the appropriate phase space. Here we have used

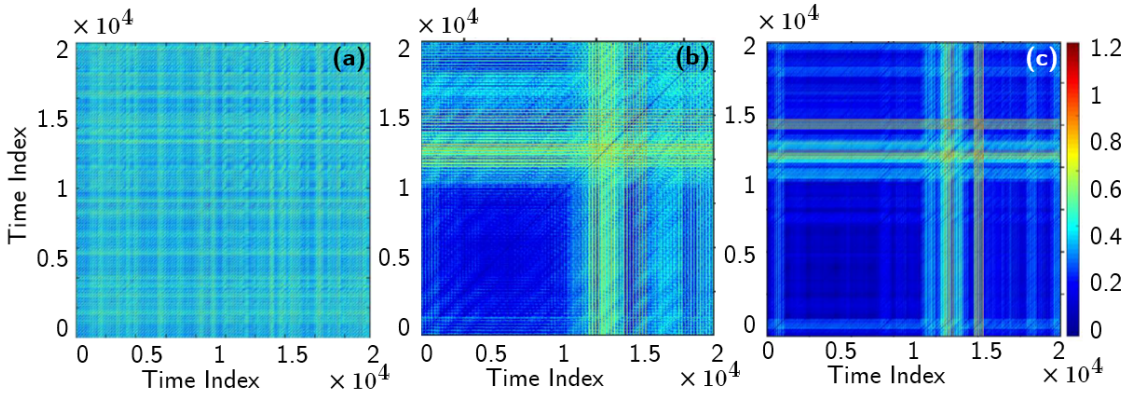

Figure 9: Recurrence Plot from (a) logistic map time series, $x(t)$ shown in Fig. 8(a); (b) shows the RP constructed from the InSync statistic, $\mathcal{I}(\hbar_k^4(t))$ calculated using all the rotation components with maximal mutual agreement, $\mathcal{G} = \{R^3(t), R^4(t), R^5(t)\}$ and (c) shows the RP of the statistic calculated using only the base component, $R^4(t)$. Here, the phase-term in the InSync statistic (Eq. (20)) is assumed equal to 1.

Table 1: Comparison of ARL1 values of EWMA, SD-WCUSUM and InSync for different values of SNR

SNR	EWMA	SD-WCUSUM	InSync
20	36.15	8.49	1.05
10	205.35	175.6*	1.05
6.67	288.43	199.68*	1.18
5	317.46	277.49*	1.73

* *failed to detect change in 10% of total runs*

an embedding dimension, $m = 3$ and time delay, $d = 10$. The RP of the original time series $x(t)$, as shown in Fig. 9(a), was not able show any discernible change in the dynamics of the process. However, the RP constructed from the InSync statistic, $\mathcal{I}(\hbar_k^4(t))$ clearly contrasts the difference between the two regimes (see Fig. 9(b)).

Also, to establish the significance of intrinsic phase and amplitude synchronization, we examine the recurrence plot constructed just from a single component, say the base component, i.e., $R^4(t)$. This is represented in Fig. 9(c). We notice that the RP does reflect some information about dynamical change, but is not able to differentiate the regime change as effectively as the RP of $\mathcal{I}(\hbar_k^4(t))$ does. This is because $R^4(t)$, or any other rotation component would contain only a fraction of the information about state change in the system. This suggests that we need to select and fuse the information contained across a set of components that are likely to preserve the information about any change in the state of the system. The information is reinforced whenever the phase and amplitude synchronization among the components is maximized, hence increasing the specificity and sensitivity of detecting the change points.

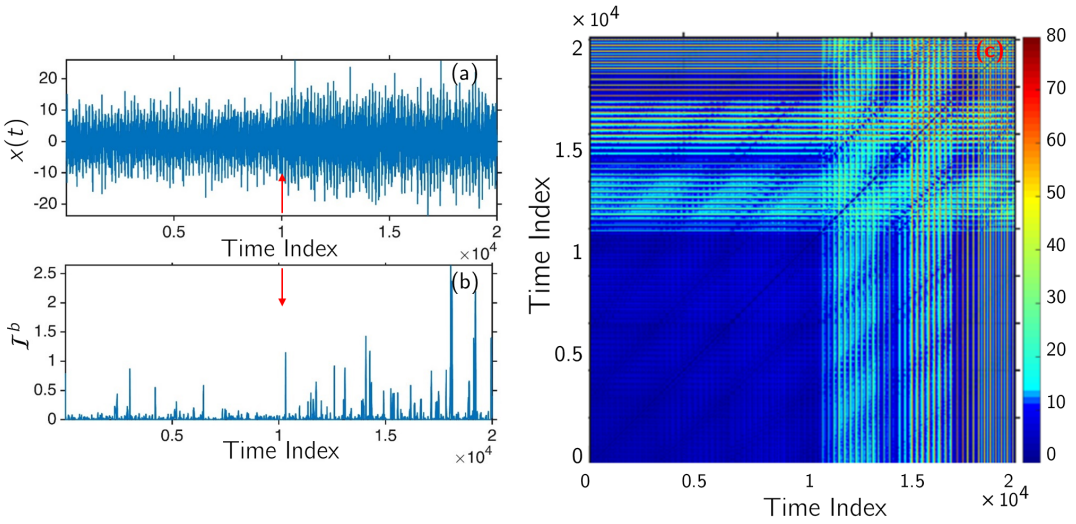

Figure 10: (a) Piecewise ARMA time series and (b)shows $\mathcal{I}(\hbar_k^3(t))$ calculated from the rotation components, $\{R^2(t), R^3(t), R^4(t)\}$ and (c) shows the RP constructed from the InSync statistic, $\mathcal{I}(\hbar_k^3(t))$.

Table 2: Comparison of ARL1 values of EWMA, SD-WCUSUM and InSync for different levels of change induced in the NVS

NVS	EWMA	SD-WCUSUM	InSync
$\{\underline{1,3,5}\} \rightarrow \{\underline{1,4,5}\}$	329	137.8*	1.28
$\{\underline{1,3,5}\} \rightarrow \{\underline{1,4,6}\}$	113.04	14.28	1.07
$\{\underline{1,3,5}\} \rightarrow \{\underline{2,4,6}\}$	109.4	6.87	1.06

* *failed to detect change in 20% of the runs*

4.2 Piecewise stationary ARMA (2,1)

In order to test the performance of the method to detect changes between two nonstationary regimes, exhibiting intermittency, we generated a time series with 20000 data points from a piecewise stationary ARMA(2,1) process with M breakpoints such that:

$$\varrho^{(m)}(B)x(t) = \Omega^{(m)}(B)w(t); t \in \mathbb{Z}; t_{m-1} \leq t < t_m \tag{23}$$

where $\varrho^{(m)}$ and $\Omega^{(m)}$ are polynomials of degree 2 and 1, respectively during m^{th} sojourn; B is the lag operator and t_m is the time index of each breakpoint, $m = 1, 2, \ldots, M; m_0 = 1, m_M = T$. The noise variance shock (NVS) when the system is in-control process, $w(t) \sim N(0, \delta\sigma^2)$ such that the variance cycles as $\delta = \{1, 3, 5, 1, 3, 5, \ldots\}$. Change in the system is introduced at $t = 10000$ by changing the amplitude of variance shock cycle as given in Table 2. Fig. 10(a) shows a representative ARMA(2,1) time series where change point is introduced by changing the NVS from $\{1, 3, 5, 1, 3, 5, ...\}$ to $\{2, 4, 6, 2, 4, 6, ...\}$. Other change points that were assessed . The sojourn time, t_m for each breakpoint is set to $t_m = 100$ data points $\forall m = 1, 2, ..., M$. The system here exhibits an intermittent behavior due to which it becomes more difficult to detect such changes. In order to visualize the changes clearly, we use RP constructed from the from InSync statistics (Fig. 10(b)) and calculate the ARL1 values. For different levels of change in noise variance shocks, the

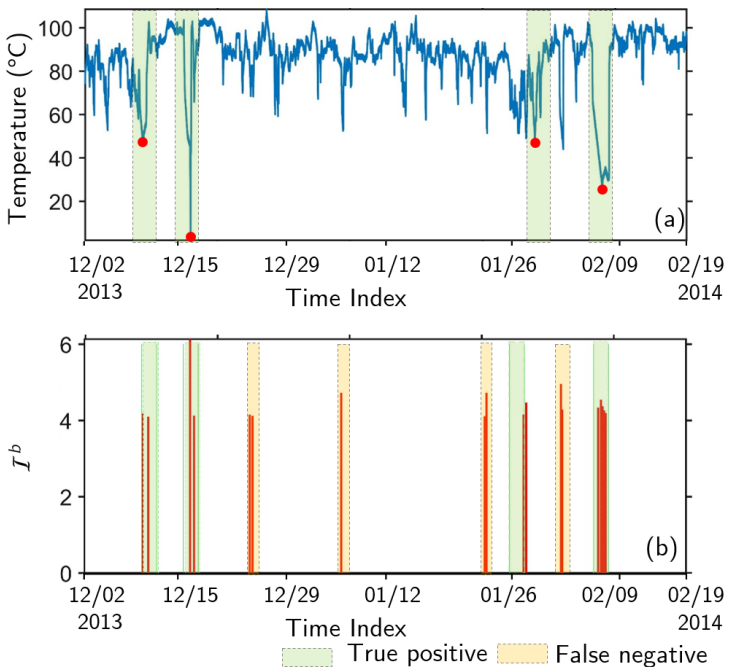

Figure 11: (a) Temperature sensor recording of an internal component of an expensive industrial machine recorded every 5 mins (b) the corresponding InSync statistic $\mathcal{I}(\hbar_k^3(t))$ calculated from the rotation components, $\{R^2(t), R^3(t), R^4(t)\}$.

ARL1 values are summarized in Table 2. We notice that in all the cases, InSync statistic was able to detect the change much earlier than EWMA and SD-WCUSUM.

4.3 Anomaly detection

To establish the effectiveness of the proposed methodology on real world non-stationary systems, we examined the benchmark dataset on anomaly detection in an expensive industrial machine inside a manufacturing plant [34]. Using an industrial temperature sensor, the temperature of an internal component of the machine was recorded every 5 min for 79 consecutive days. The temperature sensor data is shown in Fig. 11(a). The machine breaks whenever the temperature of the component abruptly goes below a specified limit. These breakdown points are marked with a circular dot in Fig. 11(a). Since the machine breaks are associated with abrupt changes, the corresponding change points are considered as points of singularity in the system. To assess the performance of various methods, a standard scoring function is proposed in [34] which is based on an anomaly window (highlighted in Fig. 11(a)) such that each window is centered around an anomaly with a specified length. A detailed description of the scoring function based on the anomaly window is presented in the Appendix F.

To detect these singularities, we analyzed the rotation components, $\{R^2(t), R^3(t), R^4(t)\}$ which forms the set with maximal mutual agreement. The InSync statistic calculated using these components detected 7 possible singularities as shown in the Fig. 11(b). As per the benchmark scoring function, if more than one anomaly is detected within the anomaly window for any change-point (regions shaded as green in Fig. 11(a)), only the first detection point is considered and the rest are ignored. Also any false positive detected close to the true positives are assigned low negative scores in comparison to the false positives which are considerably far away from the true anomaly window. We also

Table 3: Comparison of the true positives (TP), false positives (FP) and NAB benchmark score* against various benchmark methods

Methods	TP	FP	Score
InSync	**4**	**4**	**3.56**
Hierarchical Temporal Memory (HTM)	4	12	2.68
Contextual Anomaly Detector (CAD)	2	0	-0.165
Relative Entropy	2	9	-0.916
KNN-CAD	2	20	-2.856
Bayesian Change-point	1	4	-3.320

* *Maximum achievable score for this data is 4*

compared the true positives (TP) and false positives (FP) of a set of algorithms tested on this dataset along with the score function and is shown in Table 3. Notice that among all the methods, the InSync statistic is able to detect all the anomalies with relatively least number of false alarms (except the contexual anomaly detector).

Noteworthy is the point that false alarms in such industrial applications may not be completely undesirable, since it would only require the operators to put extensive checks on system monitoring.

4.4 Detecting singularities in neocortical signal

In this case study, we demonstrate the efficacy of the proposed method in detecting singularities in the signal recorded from the neocortex region of the brain. The singularities are representative of the neuronal firings in the brain and are indicative of brain responsiveness towards various sensory and spatial perception, motor commands, language etc. [35]. However, reliable and accurate detection of these spikes is still an open problem because (a) the spikes are oftentimes mistaken with other electrical activities (also referred to as volume conduction, [36]) or (b) the waiting time between two spikes may be as low as 0.6 ms, which might not be resolved by conventional change detection methods. The data in the current study is derived from [22], collected for 60 s at a sampling rate of 24k Hz. A 50 ms realization of the signal is presented in (Fig. 12(a)). Since the problem involves detecting singularities, the halfwaves containing these singularities would show a strong phase synchronization at multiple levels of $R^j(t) \in \mathcal{G}$ (see Proposition 3). To detect the spikes, first we selected the set of components with maximal mutual agreement which included $R^1(t)$ and $R^2(t)$. This is apparent since the spikes are high frequency features. The corresponding plot of the InSync statistic and the RP constructed from the InSync statistic, $\mathcal{I}(\hbar_k^1(t))$ are shown in Figs. 12(b&c), respectively. The singularity points (represented by sharp vertical lines) can be easily visualized from Fig. 12(c).

We compared the performance of the InSync statistic against the superparamagnetic clustering (SPC) algorithm proposed in [22]. The method was implemented on recordings with SNR ratio 20, 10, 6.67 and 5. To compare the performance, the number of false negative and false positive (inside bracket) are reported in Table 4. We notice that the InSync statistic was able to detect spikes in all the cases with a relatively higher sensitivity (lower false negatives) as compared to that of SPC. Since the SPC is based on identifying the shape features of spikes followed by clustering, chances are that not all the

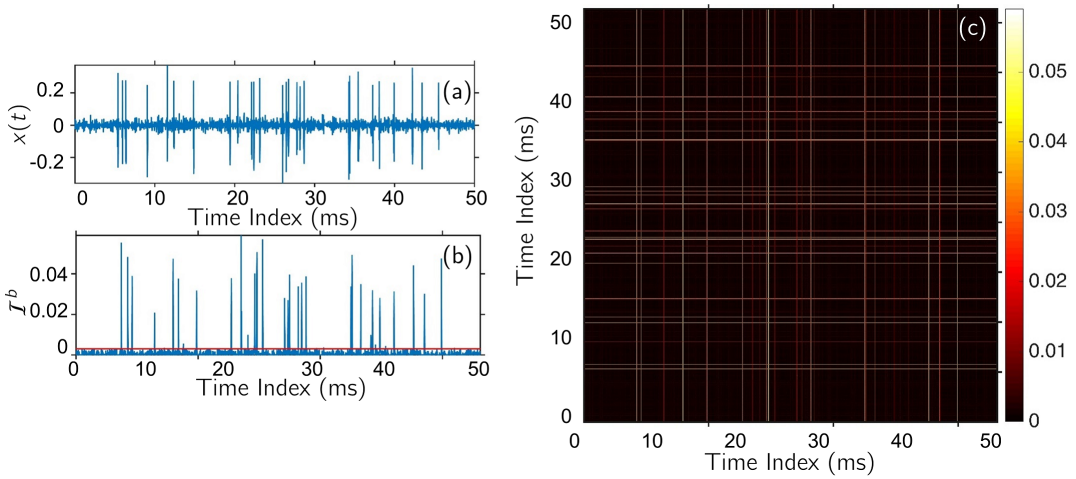

Figure 12: (a) A 50 ms realization of the neocortical recording and (b) shows the corresponding plot of the InSync statistic, $\mathcal{I}(\hbar_k^1(t))$ calculated from the rotation components, $R^1(t)$ and $R^2(t)$ (c) shows the RP constructed from the time series of $\mathcal{I}(\hbar_k^1(t))$.

Table 4: Comparison of the number of misses and false positives (inside bracket) based on a sample size of 1.44×10^6 data points against the superparamagnetic clustering (SPC) for different levels of SNR

SNR	Spike Count	SPC	InSync
20	3514	210(711)	4(8)
10	3448	179(57)	24(60)
6.67	3472	211(6)	81(96)
5	3414	403(2)	168(480)

spikes would belong to a given set of shape features. In contrast to SPC, InSync statistic directly utilizes the property of the spikes being a singularity and therefore being retained across multiple levels of rotation components with a very high probability as compared to random fluctuations.

Apparently, the false positive rate for the InSync statistic increases as the SNR decreases. This may be attributed to the fact that ITD components have the tendency to retain random fluctuations in a given signal across multiple decomposition levels—although with a very small probability (see Remark 1)—causing random fluctuations to appear as false positives in the InSync statistic. However, compared to sample size (1.44×10^6), the number of false positives would not influence the overall performance (specificity) of the InSync statistic.

5 Summary And Discussion

We have introduced an approach for change detection in nonlinear and nonstationary systems based on tracking the local phase and amplitude synchronization of multiple intrinsic components of a univariate time series signal obtained by intrinsic time scale decomposition. We showed that the signature of sharp change points, such as a singularity is preserved across multiple ITD components. Using a halfwave representation, we then

Table 5: Summary of various simulated and real world case studies implemented using the intrinsic phase and amplitude synchronization.

Case study	Change point	$\overline{\text{ARL1}}$ InSync	$\overline{\text{ARL1}}$ EWMA	$\overline{\text{ARL1}}$ SD-WCUSUM	Methods implemented and remarks
Logistic map	Periodic to chaotic	1.25	165.32	211.84	InSync consistently detected the change point with ARL1 almost 2 orders of magnitude as compared to EWMA and SD-WCUSUM.
Piecewise stationary ARMA(2,1) [9]	Change in NVS	1.13	52.98	183.82	InSync was able to detect the smallest change in NVS ($\{\underline{1,3,5}\} \rightarrow \{\underline{1,4,5}\}$) with lowest ARL1$\approx$ 1.28 in comparison to EWMA and SD-WCUSUM.
Machine temperature sensor data [34]	Machine breakdown states	1	4	4	Overall score as assigned to InSync was $\approx$ 33% higher than other benchmark methods tested. SD-WCUSUM and EWMA were able to detect the change points with sensitivity value 0.25 and high false positives resulting in an overall score of -11.5 and -4.94, respectively.
Neocortex spike detection [22]	Neuronal firings	1.05	1.25	1.30	[a]Detected spikes with maximum sensitivity (0.95) as compared to SPC (0.88) and other combinations of wavelets, K-means and PCA for spike sorting and clustering. Corresponding values of sensitivities for EWMA and SD-WCUSUM were, 0.80 and 0.77, respectively.
Obstructive Sleep Apnea (OSA), [37][b]	No OSA to OSA	1.15 ms	214 ms	193 ms	Detected the apnea onset with ARL1 $\approx$ 1.15 ms where EWMA and SD-WCUSUM detected after 214 ms and 193 ms, respectively.
Chemical Mechanical Planarization [38][b]	Pad glazing after 9 mins of polishing	6 ms	90 ms	17 ms	Pad glazing was detected by InSync statistic with ARL1 $\leq$ 6 ms as compared to 90 ms and 17 ms for EWMA and SD-WCUSUM.
Eye blinking using EEG [39][b]	Eye opening and closing events (19 events)	1.05	1.35	1.19	InSync detected the singularity events with a sensitivity value of 0.95 and 2 false positives. Corresponding values for EWMA and SD-WCUSUM were recorded to be 0.74 with 19 false positives and 0.84 with 9 false positives, respectively.

[a] *Sensitivity reported for case 4 in Table 4*
[b] *Not reported in Section 3*

defined a phase synchronization measure between halfwaves at different levels and showed that the expected level of phase synchronization about a singularity may be enhanced by at least 4 times as compared to when there is no singularity. Additionally, to select the set of ITD components which would retain the phase and amplitude information about a change, we introduced the concept of maximal mutual agreement and developed an InSync statistic that would combine and reinforce the phase and amplitude information contained across multiple levels of ITD components that are in maximal mutual agreement.

We implemented our ITD–based change detection approach on several simulated and real world case studies in neurophysiological as well as industrial settings. This included anomaly detection using time series data from machine sensor signal, singularity detection in the EEG signal collected from the neocortical region of the brain, detecting the onset of obstructive sleep apena using respiration signal and pad deterioration in chemical mechanical planarization using vibration sensor signal.

We used ARL1 values to compare the performance of our method relative to other classical approaches including EWMA and contemporary methods such as wavelet based SD-CUSUM. A summary of the performance measure is presented in Table 5. These results imply that the our method was able to detect changes in non-stationary and noisy conditions with ARL1 on an average almost 66% lower as compared to the other methods tested (based on the case studies reported in Table 5). We also showed that the sharp change points as well as the moment shifts can be detected with very high sensitivity ($\approx$ 0.91; and is almost 200% higher compared to other methods tested) and relatively lower false positive rates using the InSync statistic. The significant increase in the sensitivity of the method is attributed to its contrast enhancement property. Since the statistics combines the phase and amplitude information from multiple ITD components (which are in maximal mutual agreement), it is able to significantly enhance the contrast between different intermittent regimes and at sharp change points as evident in the recurrence plot of the InSync statistic.

Acknowledgments

This work was supported by the kind funding from National Science Foundation, grant no. CMMI-1432914, CMMI-1437139and IIP-1355765. The authors wish to thank Dr. D. Cline, Department of Statistics, Texas A&M University for suggestions on distributional approximations used in Corollary 1.

References

[1] J. Frank, S. Mannor, J. Pineau, and D. Precup, "Time series analysis using geometric template matching," *IEEE Trans. Pattern Anal. Mach. Intell.*, vol. 35, no. 3, pp. 740–754, Mar. 2013.

[2] N. E. Huang and Z. Wu, "A review on Hilbert-Huang transform: Method and its applications to geophysical studies," *Rev. Geophys.*, vol. 46, no. 2, Jun. 2008.

[3] V. Jumutc and J. A. K. Suykens, "Multi-class supervised novelty detection," *IEEE Trans. Pattern Anal. Mach. Intell.*, vol. 36, no. 12, pp. 2510–2523, Dec. 2014.

[4] A. Bulling, J. A. Ward, H. Gellersen, and G. Troster, "Eye movement analysis for activity recognition using electrooculography," *IEEE Trans. Pattern Anal. Mach. Intell.*, vol. 33, no. 4, pp. 741–753, Apr. 2011.

[5] M. Mudelsee, "Break function regression," *Eur. Phys. J. Spec. Top.*, vol. 174, no. 1, pp. 49–63, Jul. 2009.

[6] W. Taylor, "A pattern test for distinguishing between autoregressive and mean-shift data," *Taylor Enterprises, Libertyville, Illinois*, 2000. [Online]. Available: http://www.variation.com/cpa/tech/changepoint.html

[7] A. Vidal, Q. Zhang, C. Mdigue, S. Fabre, and F. Clment, "Dynpeak: An algorithm for pulse detection and frequency analysis in hormonal time series," *PLoS One*, vol. 7, pp. 1–16, Jul. 2012.

[8] C. Cheng, A. Sa-Ngasoongsong, O. Beyca, T. Le, H. Yang, Z. J. Kong, and S. T. Bukkapatnam, "Time series forecasting for nonlinear and non-stationary processes: a review and comparative study," *IIE Trans.*, vol. 47, no. 10, pp. 1053–1071, Jan. 2015.

[9] Z. Wang, S. T. Bukkapatnam, S. R. Kumara, Z. Kong, and Z. Katz, "Change detection in precision manufacturing processes under transient conditions," *CIRP Ann-Manuf. Techn.*, vol. 63, no. 1, pp. 449 – 452, May 2014.

[10] J. Gao and H. Cai, "On the structures and quantification of recurrence plots," *Phys. Lett. A*, vol. 270, no. 12, pp. 75 – 87, May 2000.

[11] L. Y. Chiang and P. Coles, "Phase information and the evolution of cosmological density perturbations," *Mon. Not. R. Astron. Soc.*, vol. 311, no. 4, pp. 809–824, Feb. 2000.

[12] A. V. Oppenheim and J. S. Lim, "The importance of phase in signals," *Proc. IEEE*, vol. 69, no. 5, pp. 529–541, May 1981.

[13] F. Varela, J. P. Lachaux, E. Rodriguez, and J. Martinerie, "The brainweb: Phase synchronization and large-scale integration," *Nat. Rev. Neurosci.*, vol. 2, no. 4, pp. 229–239, Apr. 2001.

[14] K. K. Paliwal and L. D. Alsteris, "On the usefulness of STFT phase spectrum in human listening tests," *Speech Commun.*, vol. 45, no. 2, pp. 153 – 170, Oct. 2005.

[15] M. G. Rosenblum, A. S. Pikovsky, and J. Kurths, "Phase synchronization of chaotic oscillators," *Phys. Rev. Lett.*, vol. 76, pp. 1804–1807, Mar. 1996.

[16] D. Martin, C. Fowlkes, D. Tal, and J. Malik, "A database of human segmented natural images and its application to evaluating segmentation algorithms and measuring ecological statistics," in *Proc. 8th Int'l Conf. Computer Vision*, vol. 2, July 2001, pp. 416–423.

[17] L. Cohen, *Time-Frequency Analysis: Theory and Applications.* Upper Saddle River, NJ, USA: Prentice-Hall, Inc., 1995.

[18] N. E. Huang, Z. Shen, S. R. Long, M. C. Wu, H. H. Shih, Q. Zheng, N. C. Yen, C. C. Tung, and H. H. Liu, "The empirical mode decomposition and the hilbert spectrum for nonlinear and non-stationary time series analysis," *Proc. R. Soc. A*, vol. 454, no. 1971, pp. 903–995, Mar. 1998.

[19] J. M. Hughes, D. Mao, D. N. Rockmore, Y. Wang, and Q. Wu, "Empirical mode decomposition analysis for visual stylometry," *IEEE Trans. Pattern Anal. Mach. Intell.*, vol. 34, no. 11, pp. 2147–2157, Nov. 2012.

[20] P. Gloersen and N. Huang, "Comparison of interannual intrinsic modes in hemispheric sea ice covers and other geophysical parameters," *IEEE Trans. Geosci. Remote Sens.*, vol. 41, no. 5, pp. 1062–1074, May 2003.

[21] M. G. Frei and I. Osorio, "Intrinsic time-scale decomposition: time–frequency–energy analysis and real-time filtering of non-stationary signals," *Proc. R. Soc. A*, vol. 463, no. 2078, pp. 321–342, Feb. 2007.

[22] R. Q. Quiroga, Z. Nadasdy, and Y. Ben Shaul, "Unsupervised spike detection and sorting with wavelets and superparamagnetic clustering," *Neural Comput.*, vol. 16, no. 8, pp. 1661–1687, Aug. 2004.

[23] M. O. Franz, "Volterra and wiener series," *Scholarpedia*, vol. 6, no. 10, p. 11307, 2011.

[24] J. M. Restrepo, S. Venkataramani, D. Comeau, and H. Flaschka, "Defining a trend for time series using the intrinsic time-scale decomposition," *New J. Phys.*, vol. 16, no. 8, p. 085004, Aug. 2014.

[25] J. M. Gonzalez-Miranda, "Amplitude envelope synchronization in coupled chaotic oscillators," *Phys. Rev. E*, vol. 65, p. 036232, Mar. 2002.

[26] S. Banerjee, *Chaos Synchronization and Cryptography for Secure Communications: Applications for Encryption.* Hershey, PA, USA: IGI Global, 2010.

[27] D. N. Reshef, Y. A. Reshef, H. K. Finucane, S. R. Grossman, G. McVean, P. J. Turnbaugh, E. S. Lander, M. Mitzenmacher, and P. C. Sabeti, "Detecting novel associations in large data sets," *Science*, vol. 334, no. 6062, pp. 1518–1524, Dec. 2011.

[28] J. F. Donges, Y. Zou, N. Marwan, and J. Kurths, "Complex networks in climate dynamics," *Eur. Phys. J. Spec. Top.*, vol. 174, no. 1, pp. 157–179, Jul. 2009.

[29] I. Kitov, "Modeling the evolution of age-dependent gini coefficient for personal incomes in the us between 1967 and 2005," *Available at SSRN https://ssrn.com/abstract=1231882*, Aug. 2008.

[30] J. Paret and P. Tabeling, "Experimental observation of the two-dimensional inverse energy cascade," *Phys. Rev. Lett.*, vol. 79, pp. 4162–4165, Nov. 1997.

[31] H. Guo, K. Paynabar, and J. Jin, "Multiscale monitoring of autocorrelated processes using wavelets analysis," *IIE Trans.*, vol. 44, no. 4, pp. 312–326, Jan. 2012.

[32] J.-P. Eckmann, S. O. Kamphorst, and D. Ruelle, "Recurrence plots of dynamical systems," *Europhys. Lett.*, vol. 4, no. 9, p. 973, Aug. 1987.

[33] N. Marwan, M. C. Romano, M. Thiel, and J. Kurths, "Recurrence plots for the analysis of complex systems," *Phys. Rep.*, vol. 438, no. 5, pp. 237–329, Jan. 2007.

[34] A. Lavin and S. Ahmad, "Evaluating real-time anomaly detection algorithms–the numenta anomaly benchmark," in *IEEE 14th Int. Conf. Mach. Learn. Appl.* IEEE, 2015, pp. 38–44.

[35] R. Q. Quiroga, L. Reddy, G. Kreiman, C. Koch, and I. Fried, "Invariant visual representation by single neurons in the human brain," *Nature*, vol. 435, no. 7045, pp. 1102–1107, Feb. 2005.

[36] S. Gordon, P. Franaszczuk, W. Hairston, M. Vindiola, and K. McDowell, "Comparing parametric and nonparametric methods for detecting phase synchronization in EEG," *J. Neurosci. Methods*, vol. 212, no. 2, pp. 247–258, Oct. 2013.

[37] T. Q. Le, C. Cheng, A. Sangasoongsong, W. Wongdhamma, and S. T. S. Bukkapatnam, "Wireless wearable multisensory suite and real-time prediction of obstructive sleep apnea episodes," *IEEE J. Transl. Eng. Health Med.*, vol. 1, pp. 2 700 109–2 700 109, Jul. 2013.

[38] P. K. Rao, "Sensor-based monitoring and inspection of surface morphology in ultraprecision manufacturing processes," Ph.D. dissertation, Dept. Ind. Eng. Mgmt., Oklahoma State Univ., Stillwater, OK, 2013.

[39] M. Lichman, "UCI machine learning repository," 2013. [Online]. Available: http://archive.ics.uci.edu/ml

Supplemental Material:

Appendix A

Proposition 1. *The probability that an extremum in level j is retained as an extremum in the subsequent η levels is approximately equal to* 0.24^{η}.

Proof. Let q_k^j be defined as follows,

$$q_k^j := \frac{(\tau_k^j - \tau_{k-1}^j) - (\tau_{k+1}^j - \tau_k^j)}{(\tau_k^j - \tau_{k-1}^j) + (\tau_{k+1}^j - \tau_k^j)} = \frac{\Delta_k^j - \Delta_{k+1}^j}{\Delta_k^j + \Delta_{k+1}^j} \tag{S1}$$

Based on [S1], any three consecutive extrema in level $j+1$, say, r_1^{j+1}, r_2^{j+1} and r_3^{j+1}, given the corresponding realizations of q_1^j, q_2^j and q_3^j in level j, follows a joint Gaussian distribution with joint conditional density given as,

$$f\left(r_1^{j+1}, r_2^{j+1}, r_3^{j+1} \middle| q_1^j, q_2^j, q_3^j\right) = \frac{1}{\sqrt{8\pi^3 \mathrm{Det}\left(\sum\left(q_1^j, q_2^j, q_3^j\right)\right)}} \exp\left(-\frac{1}{2}\boldsymbol{r}^{\boldsymbol{T}} \sum\left(q_1^j, q_2^j, q_3^j\right) \boldsymbol{r}\right) \tag{S2}$$

where, $\boldsymbol{r} = \left\{r_1^{j+1}, r_2^{j+1}, r_3^{j+1}\right\}$ with covariance matrix expressed as follows:

$$\sum\left(q_1^j, q_2^j, q_3^j\right) = MM^T = \begin{pmatrix} 6+2q_1^2 & 4+2q_1-2q_2 & (1+q_1)(1-q_3) \\ 4+2q_1-2q_2 & 6+2q_2 & 4+2q_2^j-2q_3 \\ (1+q_1)(1-q_3) & 4+2q_2-2q_3 & 6+2q_3^2 \end{pmatrix} \tag{S3}$$

Now, with the exponential approximation of inter-extremal separation, Δ_k^j (see Lemma 1, Appendix B), and the expression for q_k^j as given in Eq. (S1), we have

$$F_{q_1,q_2}(\omega_1, \omega_2) = \int_0^{\infty} e^{-\Delta_1+\Delta_2+\Delta_3} \left(\int_{\frac{1-\omega_1}{1+\omega_1}}^{\infty} d\Delta_1 \int_{\frac{1-\omega_2}{1+\omega_2}}^{\infty} d\Delta_3\right) d\Delta_2$$

Similarly, we get the distribution function of $F_{q_2,q_3}(\omega_2, \omega_3)$. Thus, we can deduce the joint density of q_1^j, q_2^j, q_3^j as,

$$f\left(q_1^j, q_2^j, q_3^j\right) = \frac{128\left(1-q_1^j\right)\left(1+q_2^j\right)\left(1-q_2^j\right)\left(1+q_3^j\right)}{\left(3-q_1^j+q_2^j+q_1^j q_2^j\right)^3\left(3-q_2^j+q_3^j+q_2^j q_3^j\right)^3} \tag{S4}$$

Using Eqs. (S2&S4), we have the joint distribution of $r_1^{j+1}, r_2^{j+1}, r_3^{j+1}, q_1^j, q_2^j, q_3^j$. Further assuming the marginal distribution of $r_1^{j+1}, r_2^{j+1}, r_3^{j+1}$ to be normally distributed (cf. Proposition 1), the covariance matrix can be approximated as follows:

$$\begin{aligned} \sum &= \int_{-1}^{1} dq_1^j \int_{-1}^{1} dq_2^j \int_{-1}^{1} dq_3^j \sum\left(q_1^j, q_2^j, q_3^j\right) p\left(q_1^j, q_2^j, q_3^j\right) \\ &\approx \begin{pmatrix} 0.42 & 0.25 & 0.058 \\ 0.25 & 0.42 & 0.25 \\ 0.058 & 0.25 & 0.42 \end{pmatrix} \end{aligned}$$

Thus, the marginal distribution $r_1^{j+1}, r_2^{j+1}, r_3^{j+1}$ can be represented as follows:

$$f\left(r_1^{j+1}, r_2^{j+1}, r_3^{j+1}\right) \approx \frac{1}{\sqrt{8\pi^3 \mathrm{Det}(\sum)}} \exp\left(-\frac{1}{2}\boldsymbol{r}^T\left(\sum\right)^{-1}\boldsymbol{r}\right)$$

Once we have the distribution functions, we can calculate the probability of preserving an extremum in level $j+1$ as,

$$\int_{-\infty}^{\infty} dr_3^{j+1} \int_{r_3^{j+1}}^{\infty} r_2^{j+1} \int_{-\infty}^{r_2^{j+1}} p\left(r_1^{j+1}, r_2^{j+1}, r_3^{j+1}\right) dr_1^{j+1} \approx 0.24 \tag{S5}$$

Upon generalizing Eq. (S5), we get the probability of retaining an extremum over η subsequent levels as 0.24^{η}. □

Appendix B

Property S1. *The evolution of extrema, $\{r_k^j\}_{k=1,2,\ldots,N}$ from $R^j(t)$ to $R^{j+1}(t)$ follows either a saddle-node (consecutive extrema vanishes, Fig.(S1(a)), pitch-fork (extrema on either side of a given extremum vanishes, Fig.(S1(b)) or trans-critical transition (no change in extrema, Fig. (S1(c))) and no new extremum is created [S1].*

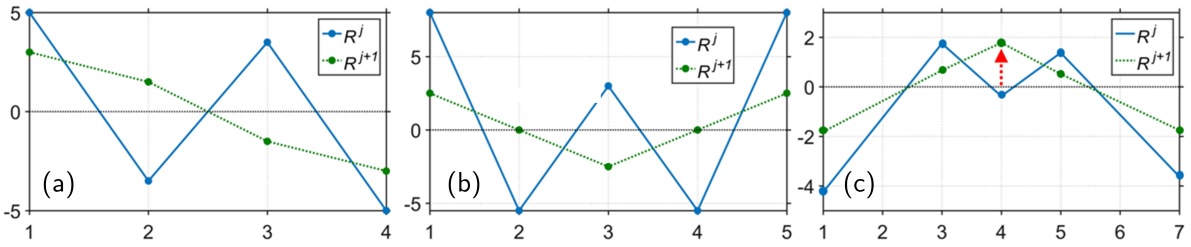

Figure S1: Evolution of extrema from $R^j(t)$ to $R^{j+1}(t)$ via (a) pitchfork (b) saddle-node and (c) trans-critical transition.

Lemma 1. *Let the inter-extremal separations be defined as $\Delta_k^j := \left(\tau_k^j - \tau_{k-1}^j\right)$. With proper continuity conditions, Δ_k^j follows an exponential distribution.*

Proof. For any level $j-1$, let the extrema locations be denoted as $\{\tau_1^{j-1}, \tau_2^{j-1}, \ldots, \tau_n^{j-1}\}$. Assuming that extrema in level j evolve independently of its neighbors, let p_τ be the probability that an extremum at τ_k^{j-1} vanishes in level j. We can see from Eqs. (S6&S7) below that the assumption here is appropriate, since the value of l_k^j governs if the extremum at τ_{k-1}^j is retained as an extremum in level j.

$$L^0(t) = x(t)$$

$$L^j(t) = l_k^j + \left(\frac{l_{k+1}^j - l_k^j}{l_{k+1}^{j-1} - l_k^{j-1}}\right)\left(L^{j-1}(t) - l_k^{j-1}\right) \tag{S6}$$

where $t \in (\tau_k^j, \tau_{k+1}^j]$ and $l_k^j (\equiv \ L^j(\tau_k^j)), \forall k = 1, 2, ..., N^j$, are the values of successive extrema at the baseline level j. The next extremum, i.e., l_{k+1}^j in Eq. (S6) can be obtained recursively as:

$$l_{k+1}^j = \frac{1}{2}\left(l_k^{j-1} + l_{k+1}^{j-1}\right) + \frac{\tau_{k+1}^{j-1} - \tau_k^{j-1}}{\tau_{k+2}^{j-1} - \tau_k^{j-1}}\left(l_{k+2}^{j-1} - l_k^{j-1}\right) \tag{S7}$$

Since the value of l_k^j is independent of τ_{k-1}^j, therefore, $\Delta_k^j = \sum_{k|\tau_k^j > \tau_k^{j-1} > \tau_{k-1}^j} \Delta_k^{j-1}$. For cardinality of the set $|\tau_k^j > \tau_k^{j-1} > \tau_{k-1}^j| = c_\tau^j >> 1$, from law of large numbers, $\Delta_k^j \approx c_\tau^j \mathbb{E}[\Delta_k^{j-1}]$ where c_τ^j is geometrically distributed, and hence Δ_k^j is geometrically distributed with parameter that depends on j.
For large values of N^j, the discrete geometric distribution can be approximated by exponential distribution as

$$F(\Delta_k^j) = 1 - \exp\left(\Delta_k^j / \lambda^j\right) \tag{S8}$$

where $\lambda^j = \mathbb{E}[\Delta_k^j]$. □

Lemma 2. *q_k^j $\forall k = 1, 2, \ldots, N; j \in J$, defined in Eq. (S1) follows a uniform(-1,1) distribution.*

Proof. Rewriting q_k^j as,

$$q_k^j = \frac{\Delta_k^j - \Delta_{k+1}^j}{\Delta_k^j + \Delta_{k+1}^j} = \frac{\Delta_k^j / \Delta_{k+1}^j - 1}{\Delta_k^j / \Delta_{k+1}^j + 1}$$

Let $V = \Delta_k^j / \Delta_{k+1}^j$. The probability density of ratio of two exponential random variables, Δ_k^j and Δ_{k+1}^j can be derived as,

$$\begin{aligned}
f_V(v) &= \int_0^\infty \rho_{k+1}^j f_{\Delta_{k+1}^j \Delta_{k+1}^j}\left(v\rho_{k+1}^j, \rho_{k+1}^j\right) d\rho_{k+1}^j \\
&= \int_0^\infty \rho_{k+1}^j (\lambda^j)^2 e^{-(\lambda^j \rho_k^j)} e^{-(\lambda^j \rho_{k+1}^j)} d\rho_k^j d\rho_{k+1}^j \\
&= \int_0^\infty (\lambda^j)^2 \rho_{k+1}^j e^{-\lambda^j \rho_{k+1}^j (1+v)} d\rho_{k+1}^j \\
&= \frac{1}{(1+v)^2}
\end{aligned}$$

where, $v \in (0, \infty)$. Since, $q_k^j = (V-1)/(V+1) \implies q_k^j \in (-1, 1)$. Using change of variables, we have the density function for q_k^j given as,

$$\begin{aligned}
f(q_k^j) &= \frac{1}{(1+v)^2}\left|\frac{dV}{dq_k^j}\right| \\
&= \frac{1}{\left(1 + \left(\frac{1+q_k^j}{1-q_k^j}\right)\right)^2} \times \frac{2}{\left(1 - q_k^j\right)^2} \\
&= \frac{1}{2}
\end{aligned}$$

Since $q_k^j \in (-1, 1)$ and $f(q_k^j) = 0.5; q_k^j \sim$ uniform(-1,1). □

Appendix C

Corollary 1. *The probability $P_e(\nu)$ in Eq. (13), with first order Gaussian approximations to the distribution function to r_k^{j+1}, can be deduced in closed form as:*

$$\hat{P}_e(\nu) = \left[1 - P\left(\mathcal{Z} \leq -\frac{\nu}{\sqrt{2}}\right)\right]^2 \tag{S9}$$

where $\mathcal{Z} \sim N(0,1)$.

Proof. From Lemma 2, the ratio distribution, q_k^j in Eq. (S1) follows a uniform$(-1,1)$ distribution, with $E(q_k^j) = 0$ and $\text{Var}(q_k^j) = 1/3$. Let the transformation, $1 \pm q_k^j \triangleq q_k^{j\pm} \sim$ uniform$(0,2)$ such that $E(q_k^{j\pm}) = 1$ and $\text{Var}(q_k^{j\pm}) = 1/3$. Here, we are interested in the Gaussian approximation of the distribution of $\{r_k^{j+1} - r_{k+1}^{j+1}\}$ for $j > 1$ where $\{r_k^{j+1}\}$'s are represented as follows:

$$r_k^{j+1} = \begin{cases} \frac{1}{4}\left(2l_k^j - (1-q_k^j)l_{k-1}^j - (1+q_k^j)l_{k+1}^j\right) & k^* - 1 > k > k^* + 1; \\ \frac{1}{4}\left(2l_k^j - (1-q_k^j)l_{k-1}^j - (1+q_k^j)l_{k+1}^j\right) + f_k & k^* - 1 \leq k \leq k^* + 1; \end{cases} \tag{S10}$$

where

$$f_k = \begin{cases} \nu\sigma/2 & k = k^* \\ -q_k^{j\pm}\nu\sigma/4 & k = k^* \mp 1 \\ 0 & \text{o.w.} \end{cases} \tag{S11}$$

such that, l_k^j's are defined as:

$$l_k^j = \frac{1}{4}\left((1-q_k^{j-1})l_{k-1}^{j-1} + 2l_k^{j-1} + (1+q_k^{j-1})l_{k+1}^{j-1}\right)$$

From the construct of q_k^j in Eq. (S1), we have $E(q_k^0) = 0$ and $\text{Var}(q_k^0) = \sigma^2$ and for simplicity, we assumed $\sigma = 1$. From Laplace's method of integral approximation and the independence of q_k^{j-1} and $(l_{k-1}^{j-1} - l_{k+1}^{j-1})$, the density function of $q_k^{j-1}(l_{k-1}^{j-1} - l_{k+1}^{j-1})$ is approximately normal with $E[q_k^{j-1}(l_{k-1}^{j-1} - l_{k+1}^{j-1})] = 0$ and $\text{Var}(q_k^{j-1}(l_{k-1}^{j-1} - l_{k+1}^{j-1})) = \text{Var}(q_k^{j-1})Var(l_{k-1}^{j-1} - l_{k+1}^{j-1}) = 2/3$. Therefore, $\text{Var}(l_k^j) = 20/48 = 5/12$.
First, we determine the distribution of r_k^{j+1} given as follows:

$$r_k^{j+1} = \frac{1}{4}\left(2l_k^j - l_{k-1}^j + l_{k+1}^j + q_k^j(l_{k-1}^j - l_{k+1}^j)\right) + f_k$$

For $k = k^*$, clearly $E(r_k^{j+1}) = \nu/2$ and the variance term is given as follows:

$$\begin{aligned} \text{Var}(r_k^{j+1}) &= \frac{1}{16}\text{Var}\left(2l_k^j - q_k^{j-}l_{k-1}^j - q_k^{j+}l_{k+1}^j\right) \\ &= \frac{1}{16}\left(\frac{20}{3}\sigma^2 - 4E(q_k^{j-})\text{Cov}(l_k^j, l_{k-1}^j) + 2E(q_k^{j-})^2\text{Cov}(l_{k-1}^j, l_{k+1}^j) - 4E(q_k^{j+})\text{Cov}(l_k^j, l_{k+1}^j)\right) \\ &= \frac{1}{16}\left(\frac{20}{3}\sigma^2 - 2 + \frac{1}{12}\right) = \frac{1}{16}\left(\frac{25}{9} - \frac{23}{12}\right) \approx \frac{1}{19} \end{aligned}$$

From Eq. (S10), we notice that, $\hat{r}_{k\pm1}^{j+1} \sim \mathcal{N}(0, 1/19)$ for $k = k^*$, $\hat{r}_{k^*}^{j+1} \sim \mathcal{N}(\nu/4, 1/19)$ $k^* - 1 > k > k^* + 1$. Call $\hat{r}_{k^*}^{j+1}$ as X Also, for $k = \{k^* - 1, k^* + 1\}$ the distribution of

$\hat{r}_{k\pm1}^{j+1}$ is equal to the sum of a $\boldsymbol{\mathcal{N}}(0, 1/19)$ and a uniformly distributed random variable, $\boldsymbol{\mathcal{U}}(-\nu/4, 0)$. Call these two random variables Y and Z. Therefore the distribution of $\hat{r}_k^{j+1} - \hat{r}_{k+1}^{j+1}$ translates to the distribution of $X - (Y + Z) \Leftrightarrow (X - Y) + Z$.
We determine the distribution of $X - Y$ first. Since these two random variables share extrema, hence are correlated. Therefore, $\mathrm{Var}(X - Y) = \mathrm{Var}(X) + \mathrm{Var}(Y) - 2\mathrm{Cov}(X, Y)$ and $E(X - Y) = \nu/4$. Here, $\mathrm{Cov}(X, Y) = E(XY)$ given as follows:

$$\begin{aligned} E(X_1X_2) &= \frac{1}{16}E(4l_k^jl_{k-1}^j - 2l_k^jl_{k-2}^j - 2l_k^jl_k^j - 2l_{k-1}^jl_{k-1}^j + l_{k-1}^jl_{k-2}^j + l_{k-1}^jl_k^j - 2l_{k-1}^jl_{k+1}^j + l_{k+1}^jl_k^j) \\ &= \frac{1}{16}\left(\frac{7}{4} - \frac{4}{16} - \frac{20}{12}\right) = -\frac{1}{96} \approx 0.01 \end{aligned}$$

Therefore, we have,

$$\mathrm{Var}(X - Y) \approx 2 \times \frac{1}{19} + 2 \times \frac{1}{96} \approx \frac{1}{8}$$

Now, the distribution of $X - Y + Z$ is nothing but the sum of $X - Y \sim \boldsymbol{\mathcal{N}}(\frac{\nu}{4}, \frac{1}{8})$ and $Z \sim \boldsymbol{\mathcal{U}}(0, \frac{\nu}{4})$. Let $X - Y = X'$. Therefore, we have to determine, $P(X' + Z > 0)$ where $P(Z > 0) = 1$. Therefore, we can write $P(X' + Z > 0)$ as the following conditional probability:

$$\begin{aligned} P(X' + Z > 0) &= P(X' + Z > 0|X' > 0)P(X' > 0) + P(X' + Z > 0|X' < 0)P(X' < 0) \\ &= P(X' > 0) + P(X' + Z > 0|X' < 0)P(X' < 0) \qquad \text{(S12)} \end{aligned}$$

For values of $\nu \leq 1$, $Var(Z) = \frac{1}{192} \leq \mathrm{Var}(X')$. Therefore, we have $P(X' + Z > 0) \approx P(X' > 0)$.
Using the convolution of uniform (Z) and normal (X') random, we can re-write Eq. (S12) as:

$$P(X' + Z > 0|X' < 0)P(X' < 0) = P(X' < 0) - P(X' + Z < 0) \qquad \text{(S13)}$$

Therefore,

$$\begin{aligned} P(X' < 0) &- P(X' + Z < 0) \\ &= \frac{\nu}{2\sqrt{\pi}}\int_{-\infty}^{0}\left(\exp\left(-\frac{\nu^2}{4}(x' - 1)^2\right) - \int_0^1 \exp\left(-\frac{\nu^2}{4}(z - x' + 1)^2\right)dz\right)dx' \qquad \text{(S14)} \\ &= \frac{\nu}{2\sqrt{\pi}}\int_{-\infty}^{0}\exp\left(-\frac{\nu^2}{4}(x' - 1)^2\right) - \frac{\sqrt{\pi}}{\nu}\left(\mathrm{erf}\left(\frac{\nu\,(x' - 1)}{2}\right) - \mathrm{erf}\left(\frac{\nu\,(x' - 2)}{2}\right)\right)dx' \end{aligned}$$

For $1 < \nu < 4$, the function $\int_0^1 \exp\left(-\frac{\nu^2}{4}(z - x' + 1)^2\right)dz$ is approximately normal and centered at 1.5 with variance approximately equal to $\mathrm{Var}(X')$. Since the first term is centered at 1, therefore the difference is non-zero. However, the magnitude of difference supported on negative x' axis is ≤ 0.02 and decays exponentially fast such that the magnitude of the difference is approximately 0 for $z \leq -0.5$. Hence the integral of the difference remains sufficiently close to zero and thus can be ignored. Therefore,

$$P(X' + Z > 0|X' < 0)P(X' < 0) \approx 0$$

Hence, we can approximate the probability, $P_e(\nu)$ as

$$\hat{P}_e(\nu) = \left(1 - P\left(\boldsymbol{\mathcal{Z}} \leq -\frac{\nu}{\sqrt{2}}\right)\right)^2 \qquad \square$$

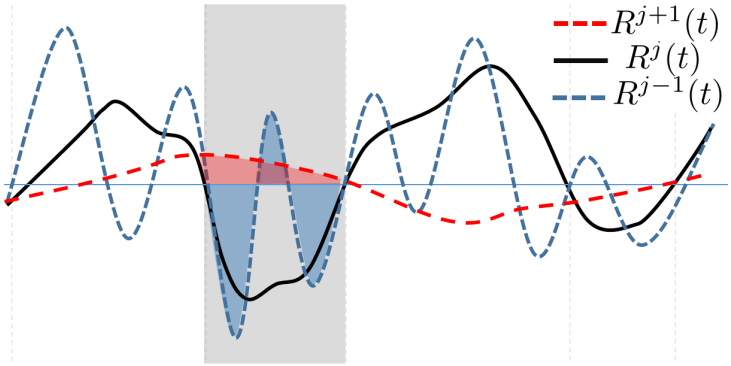

Figure S2: Illustrative example to show the halfwave span property of the rotation components, $R^j(t)$. We notice that the support of $\hbar_k^j(t)$, i.e., $(z_k^j, z_{k+1}^j]$ in $R^j(t)$ spans 3 halfwaves from the previous level, $R^{j-1}(t)$ and a fraction of halfwave from the next level rotation component, $R^{j+1}(t)$.

Appendix D

Corollary 2. *Using the Gaussian approximation to r_k^{j+1} (see Appendix C), $P_s(\nu)$ can be approximated as,*

$$\hat{P}_s(\nu) = 1 - P\left(\mathcal{Z} \leq 3 - \nu\sqrt{19/16}\right) \tag{S15}$$

Proof. Since, we have $\hat{r}_{k^*}^{j+1} \sim \mathcal{N}\left(\frac{\nu}{4}, \frac{1}{19}\right)$, therefore, $\sigma^{j+1} = \sqrt{\frac{1}{19}}\sigma^j$ and we have,

$$\begin{aligned}
\hat{P}_s(\nu) &= P(\hat{r}_{k^*}^{j+1} > 3\sigma^{j+1} | \nu \geq 3) \\
&= 1 - P\left(\mathcal{Z} \leq \frac{\left(3\sqrt{\frac{1}{19}} - \frac{\nu}{4}\right)}{\sqrt{\frac{1}{19}}}\right) \\
&= 1 - P\left(\mathcal{Z} \leq 3 - \nu\sqrt{\frac{19}{16}}\right)
\end{aligned}$$

□

Appendix E

Proposition 4 (Property 4). *The support of $\hbar_k^j(t)$ at any level $j \geq 2$ spans at least one halfwave $\hbar_k^i(t)$ from its sub-level $\{R^i(t)\}_{i<j}$ and at most one $\hbar_k^f(t)$ from its super-level $\{R^f(t)\}_{f>j}$ as shown in Fig. S2.*

Proof. Here, the support, $supp\left(\hbar_k^j(t)\right) = [z_k, z_{k+1}]$. Based on Property 5, it follows that the extrema $\{\tau_k\}_{k=1,2,\ldots,N}$ at level j evolves in level $j+1$ according to an extrema vanishing transition (saddle-node and pitchfork) or an extrema preserving transition (trans-critical and pitchfork) (cf. Fig. (13)). No new extrema are created. Therefore, $supp\left(\hbar_k^j(t)\right) \leq supp\left(\hbar_k^{j+1}(t)\right)$, and thus, $\hbar_k^j(t)$ spans at most one $\hbar_k^{j+1}(t)$ from its super-level $\{R^f(t)\}_{f>j}$. Similarly, we have $supp\left(\hbar_k^j(t)\right) \geq supp\left(\hbar_k^{j-1}\right)$ and hence $\hbar_k^j$ spans at least one $\hbar_k^{j-1}$ from its sub-level $\{R^i(t)\}_{i<j}$.

Appendix F

The performance of various anomaly detection algorithms, as proposed in [S2], is assessed based on a standard scoring function. The function assigns a weighted positive score to an algorithm that is able to detect a change within a prescribed anomaly window while penalizes for any missing anomaly. Length of the anomaly window is typically set to 10% of the length of time series.

Correctly identified anomalies are assigned a score, A_{TP} of 1 while false positives and missed anomalies are penalized with scores of $A_{\text{FP}} = 0.11$ and $A_{\text{FN}} = 1$, respectively. Depending on where the anomaly was detected with reference to the anomaly window, the reward as well as the penalty weights assigned to individual detection are determined using a scaled sigmoid function as shown in Fig. S3. From the figure we notice that a negative weight of -1 is assigned to a FP which is far from the anomaly window. In contrast, a FP is penalized less if it is closer to the window.

An illustrative example for a sample anomaly window is shown in Fig. S3. The first point is a FP preceding the anomaly window and is penalized with a weight of -1. Next, for the two detections within the anomaly window, we only count the earliest TP and is assigned a positive weight of 1. Following the anomaly window, we notice two FPs. Since the first FP is less detrimental because it is close to the window as compared to the second, hence a relatively smaller negative weight of -0.83 based on the sigmoid function is assigned to the former. In contrast, a weight of -1 is assigned to the latter because its too far from the window to be associated with the true anomaly. True negatives are assumed to make no contributions. Hence, with the scores for FP, TP and FN as mentioned earlier, the final score for the example shown in Fig. S3 is: $-1.0A_{\text{FP}} + 1A_{\text{TP}} - 0.8093A_{\text{FP}} - 1.0A_{\text{FP}} = 0.6909$.

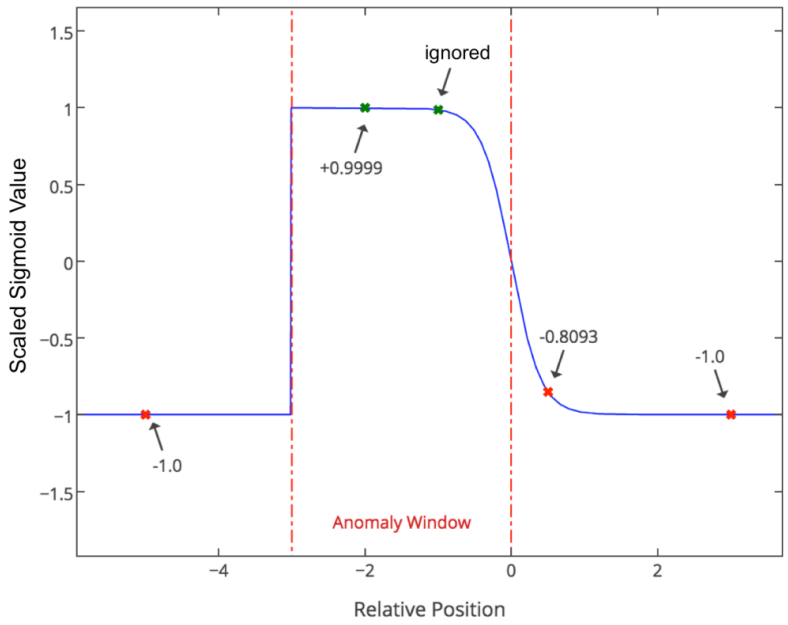

Figure S3: Scale sigmoid function to determine the score relative to the anomaly window shown by the red dotted lines. The markers represent the detections made by a sample algorithm relative to the anomaly window.

Appendix References

[S1] J. M. Restrepo, S. Venkataramani, D. Comeau, and H. Flaschka, "Defining a trend for time series using the intrinsic time-scale decomposition," *New J. Phys.*, vol. 16, no. 8, p. 085004, Aug. 2014.

[S2] A. Lavin and S. Ahmad, "Evaluating real-time anomaly detection algorithms–the numenta anomaly benchmark," in *IEEE 14th Int. Conf. Mach. Learn. Appl.* IEEE, 2015, pp. 38–44.